



### 저작자표시 2.0 대한민국

이용자는 아래의 조건을 따르는 경우에 한하여 자유롭게

- 이 저작물을 복제, 배포, 전송, 전시, 공연 및 방송할 수 있습니다.
- 이차적 저작물을 작성할 수 있습니다.
- 이 저작물을 영리 목적으로 이용할 수 있습니다.

다음과 같은 조건을 따라야 합니다:



저작자표시. 귀하는 원 저작자를 표시하여야 합니다.

- 귀하는, 이 저작물의 재이용이나 배포의 경우, 이 저작물에 적용된 이용허락조건을 명확하게 나타내어야 합니다.
- 저작권자로부터 별도의 허가를 받으면 이러한 조건들은 적용되지 않습니다.

저작권법에 따른 이용자의 권리는 위의 내용에 의하여 영향을 받지 않습니다.

이것은 [이용허락규약\(Legal Code\)](#)을 이해하기 쉽게 요약한 것입니다.

[Disclaimer](#)



이학박사 학위논문

# Geometrical Control of Terahertz Field Enhancement in Nano Gaps

나노 갭의 구조 변형을 통한 테라헤르츠  
전자기파의 전기장 집속 조절

2014년 12월

서울대학교 대학원

물리천문학부 물리학 전공

박영미

# Geometrical Control of Terahertz Field Enhancement in nano gaps

지도 교수 김 대 식

이 논문을 이학박사 학위논문으로 제출함  
2014년 12월

서울대학교 대학원  
물리천문학부 물리학 전공  
박영미

박영미의 이학박사 학위논문을 인준함  
2014년 12월

위원장 박 건식 (인)

부위원장 김 대식 (인)

위원 노태원 (인)

위원 홍승훈 (인)

위원 이상민 (인)

# Geometrical Control of Terahertz Field Enhancement in nano gaps

by

Young-Mi Bahk

Supervised by

Prof. Dai-Sik Kim

A Dissertation Submitted to the Faculty of Seoul National University  
in Candidacy for the Degree of Doctor of Philosophy

December 2014

Department of Physics and Astronomy

Graduate School

Seoul National University

## Abstract

# Geometrical Control of Terahertz Field Enhancement in nano gaps

Young-Mi Bahk

Department of Physics and Astronomy

The Graduate School

Seoul National University

In this thesis, I will demonstrate optimal design of nano gaps ( $w \ll \lambda$ ), in particular nano slot antennas and nano slits, to control field enhancement of terahertz electromagnetic waves. For the case of THz nano slot antenna which is a few hundred micrometer long rectangular hole with a nanometer sized width, we can control the interaction between nano slot antennas by transverse arrangement of rectangular holes with a different distance between two holes. Because of the nano-sized width, it is possible to realize strong coupling (short-range coupling) ( $d \sim \frac{\lambda}{100}$ ) as well as weak coupling (long-range coupling) ( $d \geq \lambda$ ). We will discuss the coupling effect which greatly affects to field enhancement of nano slot antennas. Moreover, THz nano slit with a nanometer sized width and an infinite length, in the sense of being longer than any of the wavelengths used, is a good structure to gain physical insight and achieve quantitative description of the interaction between millimeter waves with nano sized aperture. Here, we will study field enhancement of THz nano slits with a gap size down to  $w \sim \frac{\lambda}{1,000,000}$ , which is possible by successful fabrication of a single slit with a few nanometer gap size.

**Keywords** : Terahertz spectroscopy; Terahertz plasmonics;  
Subwavelength structure; Nanogap; Field enhancement; Coupling;

Student Number : 2004–20430

# Table of contents

Abstract.....	2
Table of contents.....	4
List of figures.....	6
Chapter 1 Introduction.....	11
Chapter 2 Terahertz Time domain spectroscopy.....	12
Chapter 3 Terahertz nano slot antenna and nano slit.....	15
3.1 Introduction.....	16
3.2 THz nano slot antenna.....	16
3.3 THz nano slit.....	19
Chapter 4 Control of field enhancement by coupling effect between THz nano slot antennas.....	20
4.1 Two THz nano slot antennas.....	21
4.1.1 Introduction.....	21
4.1.2 Sample fabrication.....	22
4.1.3 Single THz nano slot antennas.....	23
4.1.4 Theoretical analysis.....	24
4.1.5 Two symmetric THz nano slot antennas .....	26
4.1.6 Two asymmetric THz nano slot antennas.....	30
4.1.7 Conclusions.....	35

4.2 Array of THz nano slot antennas.....	36
4.2.1 Introduction.....	36
4.2.2 Array of THz nano slot antennas.....	37
4.2.3 Theoretical analysis.....	39
4.2.4 Conclusions.....	45
 Chapter 5 Control of field enhancement by geometries of THz nano slits.....	46
5.1 Introduction.....	47
5.2 Sample fabrication.....	47
5.3 Gap size dependence of field enhancement.....	49
5.4 Current and charge distribution of nano slit.....	54
5.5 Metal thickness dependence of field enhancement.....	57
5.6 Conclusions.....	58
 Chapter 6 Conclusions.....	59
 Bibliography.....	61
 요약(국문초록).....	67
 List of publications.....	69
 Conferences.....	71

# List of figures

**Fig. 2.1** THz far field transmission setup.....11

**Fig. 2.2** (a) Electro-optic sampling signal of THz electric field emitted from the biased GaAs in the time domain. (b) Fourier transformed spectrum of the signal presented in Fig. 2.2(a).....12

**Fig. 2.3** Schematics of a reference aperture with a substrate (typically silicon, quartz or sapphire) only (left), and with a metallic sample grown on the same substrate (right).....12

**Fig. 3.1** Geometry of a rectangular hole with a length of  $l$  and a width of  $w$ , perforated on a metallic film with a thickness of  $h$ . Red dotted area shows transmission cross-section  $\sigma_{\text{res}}$  ( $l^2$ ) of the rectangle when the sample is illuminated by horizontally polarized light with normal incidence.....16

**Fig. 3.2** (a) An SEM image of THz nano slot antenna with a length of  $150 \mu\text{m}$  and a width of  $120 \text{ nm}$ . (b) Fourier transformed spectra of the electric near field at two positions of the rectangular hole. (c) Imaging of  $x$ -component of electric near field at two resonant modes ( $0.35 \text{ THz}$  (left) and  $1.1 \text{ THz}$  (right)). (d) Schematics of the fundamental (left) and the third order mode (right).....18

**Fig. 4.1** (a) Normalized transmitted amplitude spectra measured through two types of single THz nano slot antennas with different lengths  $l = 150 \mu\text{m}$  and  $100 \mu\text{m}$ , the same width  $w = 350 \text{ nm}$ . SEM images of the samples are shown in the inset. (b) Normalized-to-area amplitudes as the same presented in Fig. 4.1(a) are calculated using the modal expansion.....23

**Fig. 4.2** Geometry of a pair of THz nano slot antennas. The

structure consists of two rectangular holes transversely aligned with a various distance  $d$ , perforated on a 200-nm-thick Au film is deposited on a 500- $\mu\text{m}$ -thick Si substrate. The two rectangles have the same length ( $l = 100 \mu\text{m}$ ) and the same width ( $w = 300 \text{ nm}$ ), illuminated by horizontally polarized light with normal incidence. ....25

**Fig. 4.3** Experimental and calculated transmission spectra of two symmetric THz nano slot antennas with different distances. SEM images of the corresponding structures are shown in the left column. The middle column shows the measured spectra. The right column shows the calculated total normalized-to-area amplitude for the corresponding  $d$ . ....27

**Fig. 4.4** Evolution of the transmission resonance amplitude normalized by that of a single rectangular hole.....28

**Fig. 4.5** Geometry of two asymmetric THz nano slot antennas which have different lengths ( $l_1 = 150 \mu\text{m}$  and  $l_2 = 100 \mu\text{m}$ ) and the same width ( $w = 350 \text{ nm}$ ). Two rectangular holes are separated with a various distance  $d$ , and illuminated by horizontally polarized light with normal incidence.....29

**Fig. 4.6** Transmission spectra for two asymmetric THz nano slot antennas in dependence on the distances  $d$ . SEM images (left column), the measured spectra (middle column), and the theoretical calculations (right column) of the corresponding structures are shown in the figure. ....31

**Fig. 4.7** Evolution of the two resonant transmission normalized by the respective maximum transmission of a single slot antenna as a function of  $d$ .....32

**Fig. 4.8** Evolution of imaginary parts of the averaged EM coupling

$$\text{between two holes, } G_{\alpha\beta}^{\text{ave}} = \frac{G_{\alpha\beta}^I + G_{\alpha\beta}^{III}}{2} \quad \text{calculated at resonance 1}$$

and resonance 2.....33

**Fig. 4.9** (a) Schematic of an periodic array of slot antennas. (b) SEM images of array of THz nano slot antennas with different periods,  $d_x = 200 \mu\text{m}$  (top),  $20 \mu\text{m}$  (middle) and  $2 \mu\text{m}$  (bottom).....36

**Fig. 4.10** (a) Normalized transmitted amplitudes with varying the periods from  $d_x = 200 \mu\text{m}$  to  $d_x = 2 \mu\text{m}$ . (b) Corresponding field enhancements as a function of frequencies. The inset of the figure shows the field enhancement of the sample with  $d_x = 2 \mu\text{m}$ .....37

**Fig. 4.11** Schematic cross-sectional view of an array of rectangular holes. The different terms appearing in the equation are also schematically depicted. ....39

**Fig. 4.12** Schematic of collective re-illumination term  $S^{I,III}$ .....39

**Fig. 4.13** Experimental data (a) and calculated results (b) of field enhancement for various samples of periodic THz nano slot antenna array.....40

**Fig. 4.14** Imaginary and real parts (shown as blue lines and red lines, respectively) of the EM coupling between two holes,  $G_{0l}$ . The two slot antennas labeled with 0 and 1 have same length of  $100 \mu\text{m}$  and same width of  $200 \text{ nm}$  with a distance of  $x$ . We consider freestanding films to simplify the analytical study ( $(G_{0l})^I = (G_{0l})^{III} = G_{0l}$ ).....41

**Fig. 4.15** (a–b) Calculated real and imaginary parts, respectively, of  $S$  versus the number of holes  $N$ . All the magnitudes shown in this figure are evaluated at the resonance frequency of a single hole,  $f_{\text{res}} = 1.43 \text{ THz}$  ( $\lambda_{\text{res}} = 209 \mu\text{m}$ ). (c) Maximum normalized-to-area

transmission  $T_{\max}$  versus the number of apertures computed for the different values of  $d_x$  considered in (a) and (b). Inset displays the case corresponding to  $d_x = 202 \mu\text{m}$ . Dashed gray line in main figure corresponds to the value of  $T_{\max}$  for a single isolated hole. ....42

**Fig. 5.1** Atomic layer lithography. A patterned metal film is coated by  $\text{Al}_2\text{O}_3$  using ALD. A secondary metal is deposited on the same sample and an adhesive tape is applied to remove the second metal selectively.....47

**Fig. 5.2** Schematic of a single slit with a various gap size  $w$  from 50  $\mu\text{m}$  down to 1 nm, on an Au film deposited on a sapphire substrate (thickness of 650  $\mu\text{m}$ ). The thickness of Au film ( $h$ ) is 200 nm which is covering the aspect ratio  $h / w$  from  $10^{-3}$  up to  $10^2$ .....48

**Fig. 5.3** (a–c) Top view of SEM images for single slits with three different gap sizes ( $w = 2 \mu\text{m}$  (a), 200 nm (b) and 2 nm (c)). (d–f) cross-sectional view of single slits fabricated with atomic layer lithography ( $w = 5 \text{ nm}$  (d), 2 nm (e) and 1 nm(f)). (g–h) Tilted view (g) and TEM image (h) of 1 nm gap.....49

**Fig. 5.4** (a) Time traces of transmitted THz electric field through a single slit with 5 nm gap and bare sapphire for reference. (b) Normalized amplitude and field enhancement of 5 nm gap as a function of frequency. The dotted line indicates a  $1 / f$  dependence.....50

**Fig. 5.5** Field enhancement as a function of gap size at various frequencies. The dotted lines are experimental data and the solid lines are theoretical calculation based on PEC model.....51

**Fig. 5.6** Field enhancement as a function of gap size at 0.3 THz. The dotted lines distinguish three regimes by fitting the experiment data with different gap size dependence parameter (constant,  $1/w$  and

$1/\sqrt{w}$ ) ..... 53

**Fig. 5.7** FDTD simulation of horizontal electric (a) and magnetic (b) field distributions around a nano gap with  $w = 1$  nm and  $h = 200$  nm. The wavelength is 1 mm (0.3 THz) ..... 54

**Fig. 5.8** FDTD simulation of current distribution inside metal for  $w = 200$  nm (a) and  $w = 1$  nm. (b). The metal (Au) thickness  $h$  is 200 nm ..... 55

**Fig. 5.10** Field enhancement as a function of metal thickness for 5 nm gap at 0.3 THz. The red line is theoretical calculation based on perfect electric conductor model ..... 56

# Chapter 1 Introduction

Light confinement at nanoscale has been achieved with diverse artificial metallic nanostructures such as nano gaps<sup>1-3</sup>, nano particles<sup>4,5</sup>, nano antennas<sup>6-11</sup> and so on in a wide spectral range from visible to microwave. The enhanced fields that are orders of magnitude larger than the incident field have applications in nonlinear optics and nanophotonics. Since metals become better as we move to longer wavelengths, it has benefit to confine electromagnetic energy in metallic nano gaps with infrared and terahertz (THz) waves, leading to a huge field enhancement<sup>12-14</sup>. In addition, squeezing of THz waves through only the gap without any stray facilitates strong light matter interaction with transient strong electric fields<sup>14-16</sup>.

On the other hand, THz frequency range lies between optics and electronics, and THz frequencies are the lowest frequencies in which free space conventional optics can still be used before microwave components take over. Owing to its large wavelength, deep subwavelength phenomena from  $\lambda / 100$  down to  $\lambda / 1,000,000$  are experimentally accessible<sup>1,2</sup>. In addition, THz electromagnetic waves have attracted a great deal of interest because of novel spectroscopy and imaging application as well as its capability to control low energy excitation dynamics on sub-picosecond time scale. However, it is extremely challenging to confine THz waves to a nanometer scale with fabrication of nano gaps and measure the fields in the gaps. In this thesis, we have demonstrated control of the THz field enhancement by geometry parameters of THz nano gaps which is changed from  $\sim 10^2$  nm down to 1 nm.

# Chapter 2 Terahertz Time domain spectroscopy

We perform transmission-type terahertz (THz) far field time domain spectroscopy with single-cycle THz source generated from a 2 kV/cm biased semi-insulating GaAs emitter<sup>17</sup> as shown in Fig. 2.1. The emitter is illuminated by a femtosecond Ti:sapphire laser (MIRA, Coherent) pulse train of a center-wavelength 780 nm, a 76 MHz repetition rate and a 130 fs pulse width. An electro optic sampling method is used to detect the transmitted THz waves in the time domain, in which an optical probe pulse undergoes a slight polarization rotation by the synchronized THz beam in a (110) oriented ZnTe crystal, detecting the horizontal electric field<sup>18,19</sup>. The spot size of THz wave at the focus point is about 3 mm, obtained by knife-edge experiment. In Fig. 2.2(a), the measured THz electric field amplitude is plotted in time domain. When we consider the phase retardation due to the THz induced birefringence in the detection crystal (ZnTe) and THz beam size, the maximum THz electric field can be extracted with 30 V/cm at the focus. By Fourier-transforming the time domain data, the amplitude spectrum is obtained as shown in Fig. 2.2(b). In our setup, the spectrum of the emitted THz wave spans from 0.01 THz to 2 THz.

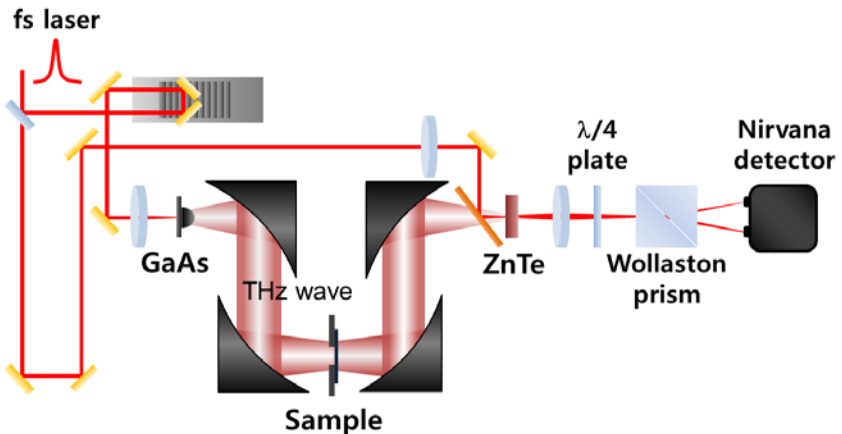
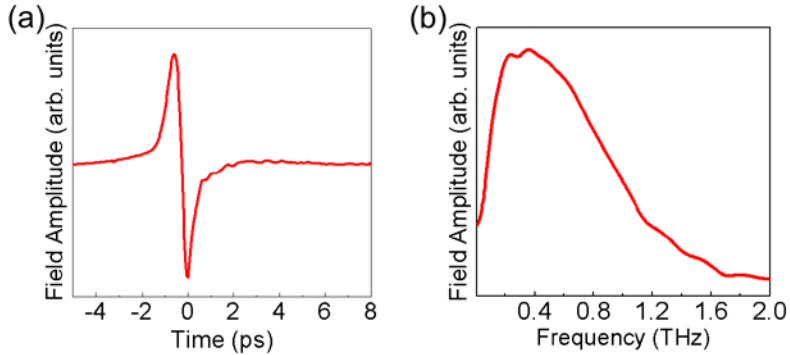


Fig. 2.1 THz far field transmission setup.



**Fig. 2.2** (a) Electro-optic sampling signal of THz electric field emitted from the biased GaAs in the time domain. (b) Fourier transformed spectrum of the signal presented in Fig. 2.2(a).

To characterize the transmission properties of our samples, we obtain the normalized transmitted amplitude  $t(\omega)$  as follows,

$$t(\omega) = \frac{|E_{\text{sample}}(\omega)|}{|E_{\text{ref}}(\omega)|} \quad (2.1).$$

where  $E_{\text{sample}}(\omega)$  and  $E_{\text{ref}}(\omega)$  are the transmitted electric field amplitude for our sample and the bare substrate after passing through a 1 mm by 1 mm metal aperture as shown in Fig. 2.3.

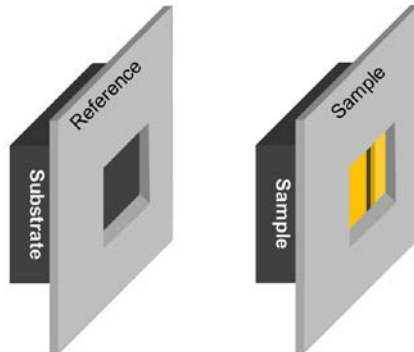


**Fig. 2.3** Schematics of a reference aperture with a substrate (typically silicon, quartz or sapphire) only (left), and with a metallic sample grown on the same substrate (right).

The transmitted far field amplitude is connected to the enhanced near field amplitude at the gap through Kirchhoff integral formalism<sup>2,20,21</sup>. When an observation point is located far from the hole, the electric field can be approximated by the Kirchhoff integral,

$$\vec{E}(\vec{r}) = \frac{ie^{i\vec{k}\cdot\vec{r}}}{2\pi r} \vec{k} \times \int_A \hat{n} \times \vec{E}(\vec{r}') e^{-i\vec{k}\cdot\vec{r}'} da' \quad (2.2),$$

where  $\vec{r}'$  is the coordinate of the element of the surface area of the hole,  $A$ ,  $r$  is the distance from origin, O, to the observation point,  $\hat{n}$  is the surface normal, and  $\vec{k}$  is the wave vector in the direction of the observation point. For an incident beam polarized in the horizontal direction and impinging upon the hole at the normal incidence, we can use the scalar expression and define the diffracted horizontal component of electric fields

$$E^{far} = \frac{e^{ikr}}{i\lambda r} \int_A E^{near}(r') da' = \frac{e^{ikr}}{i\lambda r} \langle E^{near} \rangle A \quad (2.3),$$

where the bracket means the averaged near field over the hole area, i.e.

$$\langle E^{near} \rangle = \frac{1}{A} \int_A E^{near}(r') da' \quad (2.4).$$

According to this formalism, the transmitted far field through the hole is proportional to the near field distribution inside the hole. Therefore, the near field enhancement can be estimated from the far field measurement, corresponding to  $t(\omega) / \beta$ , where  $\beta$  is the hole-to-aperture area ratio.

## Chapter 3 Terahertz nano slot antenna and nano slit

### 3.1 Introduction

Electromagnetic (EM) waves generally transmit through a single deep subwavelength hole with efficiency below unity. This low transmission efficiency is due to poor coupling of subwavelength hole with radiative EM modes and the evanescent decay of the EM fields inside the holes<sup>22,23</sup>. However, the enhanced transmission in subwavelength holes could be achieved by a bound cavity mode that couples resonantly to incident light or periodic corrugations of holes<sup>24-27</sup>. The transmission characteristics of light through various subwavelength holes and hole arrays in a metallic film have been the focus of much research activity around the world<sup>28-32</sup> and it has been proved that the hole shape influences the optical transmission properties.

### 3.2 THz nano slot antenna

Both the square hole and circular hole are poor antennas and their singularities are of an integrable kind, which limits the field enhancements<sup>24</sup>. One way to dramatically increase the field enhancement is to make the aperture a strongly asymmetric rectangle, which supports a well-defined transmission resonance for light polarized along its short side. F. J. Garcia-Vidal *et al.* have shown numerically that a single rectangular hole exhibits strong transmission resonances, its spectral location appearing close to the cutoff wavelength of the hole waveguide<sup>24</sup>. Figure 3.1 shows schematically the system: a rectangular hole with a length of  $l$  and a width of  $w$  perforated on a metallic film with a thickness of  $h$ . The structure is illuminated by  $p$ -polarized light and the metal is treated as a perfect electric conductor (PEC), a good approximation in the terahertz (THz) frequency regime. Interestingly, the maximum as the ratio  $l / w$  increases, the transmission peak develops close to the

cut-off wavelength ( $\lambda_c = 2l$ ), with increasing maximum transmittance and decreasing linewidth of the spectrum. The physical origin of the transmission resonances appearing at  $\lambda_{\text{res}} = \lambda_c$  stems from the excitation of a Fabry–Perot resonance in which the propagation constant is zero. An analytical approximation for the transmittance  $T_{\text{res}}$  and electric field enhancement  $E_{\text{res}}$  at the resonance can be obtained by

$$T_{\text{res}} \approx \frac{3}{4\pi} \frac{\lambda_{\text{res}}^2}{l \times w} \approx \frac{l^2}{l \times w} = \frac{\sigma_{\text{res}}}{A} \quad (3.1),$$

$$E_{\text{res}} \approx \frac{3}{8\sqrt{2}} \frac{\lambda_{\text{res}}^2}{l \times w} \approx \frac{l^2}{l \times w} = \frac{\sigma_{\text{res}}}{A} \quad (3.2),$$

where  $\sigma_{\text{res}}$  is a resonant transmission cross-section area of the slot antenna and  $A$  is an area of the slot antenna. This equation implies that EM energy and electric field of the dotted area ( $l^2$ ) in Fig. 3.1 can be funneled into the rectangular hole. A close analogy is found in a bound charges with losses only though radiation, whose resonant cross-section is also proportional to  $\lambda_{\text{res}}^2$ ,  $\sigma_{\text{res}} \approx \frac{3}{2\pi} \lambda_{\text{res}}^2$ .

The cross-section of the rectangular hole is half this value because we are only looking at the transmission, not reflection. The electric field enhancement has also the form resembling  $T_{\text{res}}$ , because both energy and amplitude enhancements are essentially the same, the magnetic field amplitude being almost identical to the incident one.

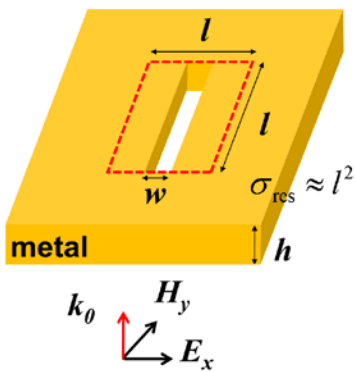


**Fig. 3.1** Geometry of a rectangular hole with a length of  $l$  and a width of  $w$ , perforated on a metallic film with a thickness of  $h$ . Red dotted area shows transmission cross-section  $\sigma_{\text{res}}$  ( $l^2$ ) of the rectangle when the sample is illuminated by horizontally polarized light with normal incidence.

THz nano slot antennas can be defined by a rectangular hole with a few hundred micron length and a nano-sized width in a thin metallic film, tailored to work as resonators in the THz frequency regime. The metal thickness is in a skin depth regime. THz nano slot antennas with a striking aspect ratio funnel THz EM waves through, accompanied by a large field enhancement unavailable for micron-sized width. Furthermore, the slot antennas with giant field enhancement open a strong possibility of potential applications, such as broadband field enhancement and nonlinear devices, filters, detectors and active switching device<sup>41-44</sup>.

Figure 3.2(a) shows a scanning electron microscope (SEM) image of a single THz nano slot antenna with a length of 150  $\mu\text{m}$  and a width of 120 nm. The sample is grown on a 300- $\mu\text{m}$ -thick (110) oriented GaP electro optic detection crystal to measure the  $x$ -component of the electric near field. Figure 3.2(b) (top) shows the spectra of the electric field at two positions of the rectangular hole. The green (blue) line is extracted from the signal at the center (edge) of the rectangle, showing a strong resonant transmission peak at 0.35 THz and a weak resonance at 1.1 THz. These peaks originate from a fundamental (0.35 THz) and a third order mode (1.1 THz) of the rectangular hole. Figure 3.2(c) and (d) show the experimental results of the electric near field imaging and the schematics of the resonance modes at two different frequencies (0.35 THz (left) and 1.1 THz (right)), respectively. From these figure, it is clear that the fundamental mode of the rectangular hole is dominant in the transmission spectrum.

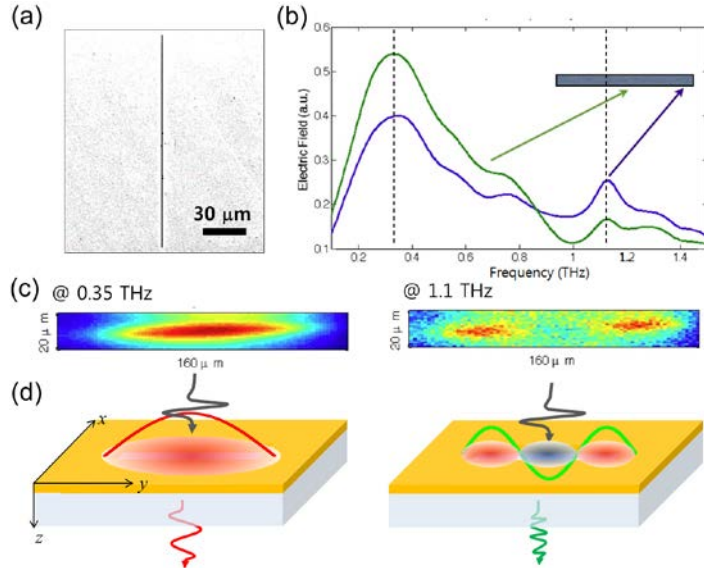


**Fig. 3.2** (a) An SEM image of THz nano slot antenna with a length of 150  $\mu\text{m}$  and a width of 120 nm. (b) Fourier transformed spectra of the electric near field at two positions of the rectangular hole. (c) Imaging of  $x$ -component of electric near field at two resonant modes (0.35 THz (left) and 1.1 THz (right)). (d) Schematics of the fundamental (left) and the third order mode (right).

### 3.3 THz nano slit

THz nano slit is a nanogap with an infinite length and a nano-sized width, leading to a huge field enhancement inside the gap. It is found that the transmittance keeps increasing with decreasing frequency, with  $1/f$  dependence<sup>2</sup> where  $f$  is frequency. With the broad spectral response, the field enhancement can reach up to a few thousands and be applied to THz nonlinearity, small THz signal detection in astronomy and for surface enhanced Raman scattering. In addition, the slit structure is a simple one dimensional system which gives to us a physical insight to understand funneling phenomena in THz nano structures. The physical understanding of funneling in THz nano slits will be studied in chapter 5.

Chapter 4 Control of field enhancement by coupling effect between THz nano slot antennas

## 4.1 Two THz nano slot antennas

### 4.1.1 Introduction

The transmission characteristics of electromagnetic (EM) waves through various subwavelength holes have been studied theoretically and experimentally since the extraordinary optical transmission phenomenon was reported over a decade ago by Ebbesen *et al.*<sup>29–32,45</sup>. It has been shown that the interaction between individual elements in an array structure strongly affects the resonance properties, resulting in spectral peak position shifts and the linewidth changes relative to that of a single structure. Since then, strongly coupled systems with various geometries have attracted considerable attention in the past few years in a wide spectral range from terahertz (THz) to visible frequencies<sup>11,46–58</sup>. Furthermore, by breaking the geometrical symmetry of the coupled structure, new electromagnetic properties, such as achieving resonances with high-quality factors and directional scattering and chirality, were observed due to asymmetric mutual interaction<sup>6,10,59–76</sup>. On the other hand, there have been many research works about applications of THz nano slot antennas with a few hundred nanometer-sized width and desired resonance properties<sup>2,42–44,77–80</sup>. Therefore, the study about coupling effect of slot antennas is worth to design and optimize the structures for specific application conditions.

There are two kinds of coupling effects. One is the longitudinal coupling which is controlled by the distance between two slot antennas along the long side of rectangular holes. In this case, the coupling effect is negligible when the length of the metal barrier is above the skin depth of the metal. On the other hand, the transverse coupling severely influences on the transmission properties of slot antennas because the overlap of the cross-section areas of two slots is sensitively changed by the distance

between two slots antennas along the short side of the rectangle. In this chapter, we will study transmission characteristics of coupled two symmetric and asymmetric THz nano slot antennas transversely aligned.

### 4.1.2 Sample fabrication

THz nano slot antennas are patterned on thin metal films by electron-beam lithography. First, negative photoresist (PR) is spin-coated on a silicon (Si) substrate with a thickness of 500  $\mu\text{m}$  and baked. Then, the desired area of the baked PR is exposed by scanning electron beam with the lithography program. After removing the un-illuminated area by development, 200-nm-thick gold (Au) films with 5-nm-thick chromium (Cr) adhesion layers are deposited on the sample. Finally, THz nano slot antennas can be made after lift-off process. The limit of pattern size is determined by the spin-coated PR and the deposited metal thickness as well as electron beam resolution. In order to obtain high signal-to-noise ratio, the structure is cloned 6 times in the direction of the length side of slot antennas with a separation (center to center) of 160  $\mu\text{m}$ . Notice that the coupling effect along the long side of the rectangular hole can be negligible because the length of the metal barrier is 10  $\mu\text{m}$  which is much larger than skin depth of Au in the THz frequency regime ( $\delta_{\text{Au}} \sim 100 \text{ nm at } 1 \text{ THz}$ ).

### 4.1.3 Single THz nano slot antennas

We begin with the investigation of transmission properties of single THz nano slot antennas<sup>78,79</sup>. Figure 4.1(a) shows experimental results of the transmission through two kinds of single slot antennas with a fixed width  $w$  of 350 nm and different lengths  $l$  of 150  $\mu\text{m}$  and 100  $\mu\text{m}$ . Scanning electron microscope (SEM) images of these samples are shown in the inset of the same figure. The maximum normalized amplitude  $t$  of two samples show about 4.3% and 2.6% even though the ratios of total area covered by the holes  $\beta$  are 0.03% ( $= (150 \mu\text{m} \times 350 \text{ nm} \times 6) / (1\text{mm} \times 1\text{mm})$ ) and 0.02% ( $= (100 \mu\text{m} \times 350 \text{ nm} \times 6) / (1\text{mm} \times 1\text{mm})$ ) for a 1mm by 1mm aluminum aperture, respectively. This is because the electric field inside rectangular hole with nano-sized width can be enhanced up to two orders of magnitude higher than the incident field<sup>78,79</sup>. The estimated field enhancement factors  $t / \beta$  are about 140 and 120 for 150- $\mu\text{m}$ -, and 100- $\mu\text{m}$ -long rectangular holes, respectively. The resonance frequencies are located at 0.4 THz and 0.6 THz for 150- $\mu\text{m}$ -, and 100- $\mu\text{m}$ -long rectangular holes, respectively. These resonance frequencies are approximately the cutoff waveguide frequencies,  $\sim c/(2n_{\text{eff}}l)$ , where  $c$  the speed of light in vacuum and  $n_{\text{eff}}$  is the effective refractive index of the substrate<sup>77</sup> ( $n_{\text{eff}} \sim 2.5$  for a Si substrate). Normalized-to-area amplitudes obtained by the numerical calculations based on the modal expansion are shown in Fig. 4.1(b) and in good agreement with the experimental results<sup>24</sup>. The normalized-to-area amplitude is corresponding to the average enhancement of electric field inside the hole. The discrepancy between the experimental and theoretical spectra may be caused by several reasons such as sample imperfections (Au roughness and structure profile) and the perfect electrical conductor (PEC) approximation in the calculations.

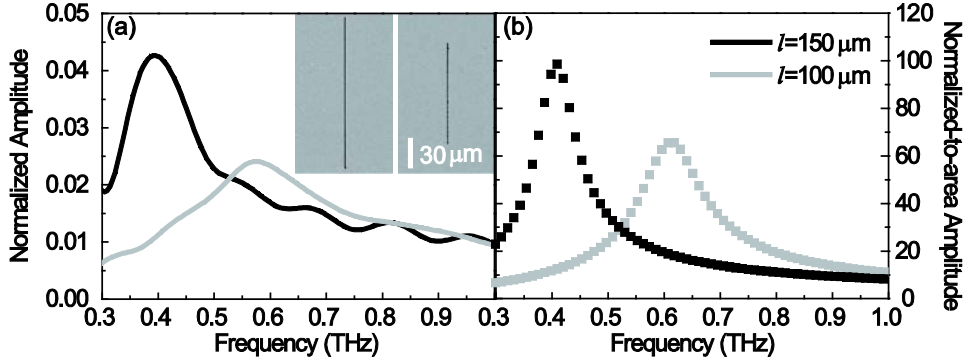


**Fig. 4.1** (a) Normalized transmitted amplitude spectra measured through two types of single THz nano slot antennas with different lengths  $l = 150\text{ }\mu\text{m}$  and  $100\text{ }\mu\text{m}$ , the same width  $w = 350\text{ nm}$ . SEM images of the samples are shown in the inset. (b) Normalized-to-area amplitudes as the same presented in Fig. 4.1(a) are calculated using the modal expansion.

#### 4.1.4 Theoretical analysis

To understand transmission properties of two slot antennas, we have applied a theoretical coupled-mode formalism based on the modal expansion of the EM fields in the different regions of the structure. A detailed account of the formalism can be found in references<sup>84</sup>. The modeling of the system ends up with solving a 4 by 4 matrix for  $E_\alpha^I$  and  $E_\alpha^{III}$  which are the modal amplitudes of the electric field at the input and output sides of the  $\alpha^{\text{th}}$  ( $\alpha = 1$  and 2) hole, respectively:

$$\begin{pmatrix} G_{11}^I - \Sigma_1 & -G_1^V & G_{12}^I & 0 \\ -G_1^V & G_{11}^{III} - \Sigma_1 & 0 & G_{12}^{III} \\ G_{21}^I & 0 & G_{22}^I - \Sigma_2 & -G_2^V \\ 0 & G_{21}^{III} & -G_2^V & G_{22}^{III} - \Sigma_2 \end{pmatrix} \begin{pmatrix} E_1^I \\ E_1^{III} \\ E_2^I \\ E_2^{III} \end{pmatrix} = \begin{pmatrix} I_0 \\ 0 \\ I_0 \\ 0 \end{pmatrix} \quad (4.1).$$

In this equation, the magnitudes  $\Sigma_\alpha$  and  $G_\alpha^V$  are defined as  $\Sigma_\alpha = Y_\alpha / \tan(q_z^\alpha h)$  and  $G_\alpha^V = Y_\alpha / \sin(q_z^\alpha h)$ , respectively,  $Y_\alpha = q_z^\alpha / k_0$  where  $k_0 = 2\pi / \lambda$  and  $q_z^\alpha = \sqrt{k_0^2 - (\pi/l_\alpha)^2}$  is the propagation constant of the fundamental TE mode inside the holes, is the admittance of the plane wave.  $\Sigma_\alpha$  is related to the bouncing back and forth of the EM fields inside an object  $\alpha$  and  $G_\alpha^V$  reflects the coupling between the EM fields at the two sides of the object.  $I_\alpha = 4\sqrt{2}/i\pi$  represents the direct illumination over an object  $\alpha$ . The terms  $G_{\alpha\beta}^{I,III}$  take into account the EM coupling between the rectangles  $\alpha$  and  $\beta$ , occurring at the two interfaces of the structure:

$$G_{\alpha\beta}^{I,III} = \frac{i}{(2\pi)^2} \frac{w_\beta l_\beta}{2} \iint dk_x dk_y \frac{k_x^2 + k_{I,IIIz}^2}{k_0 k_{I,IIIz}} F_\alpha(k_x, k_y) F_\beta(k_x, k_y) e^{-ik_x(x_\beta - x_\alpha)} e^{-ik_y(y_\beta - y_\alpha)} \quad (4.2),$$

$$F_\alpha(k_x, k_y) = \sin c\left(\frac{w_\alpha k_x}{2}\right) \left[ \sin c\left(\frac{\pi}{2} + \frac{l_\alpha k_y}{2}\right) + \sin c\left(\frac{\pi}{2} - \frac{l_\alpha k_y}{2}\right) \right] \quad (4.3),$$

where  $k_{I,IIIz} = \sqrt{\epsilon_{I,III} k_0^2 - k_x^2 - k_y^2}$  and  $l_\alpha$  and  $w_\alpha$  are the length and width, and  $(x_\alpha, y_\alpha)$  is the position of the rectangle  $\alpha$ . These propagators take into account that the point in object  $\beta$  emits EM radiation which can be collected by object  $\alpha$  ( $G_{\alpha\alpha}^{I,III}$  is related to the self-illumination of the hole.). Notice that  $\text{Re}(G_{\alpha\beta}^{I,III})$  result from the coupling of the fundamental TE mode with the *evanescent* modes at the two regions and  $\text{Im}(G_{\alpha\beta}^{I,III})$  from the *radiative* modes. When the thickness  $h$  of metal film is very thin ( $q_z^\alpha h \ll 1$ ),  $G_\alpha^V$ ,  $\Sigma_\alpha$ , and  $G_{\alpha\alpha}^{I,III}$  can be approximated to

$$G_\alpha^V \approx \frac{\lambda}{2\pi h} \gg 1, \quad \Sigma_\alpha \approx G_\alpha^V, \quad \frac{G_{22}^{I,III}}{G_{11}^{I,III}} \approx \frac{w_2 l_2}{w_1 l_1} \quad (4.4),$$

so that at each resonance the modal amplitudes of the transmitted electric field at two apertures simplify to

$$|E_1^{III}| \approx \frac{I_0}{2 \text{Im}(G_{11}^{ave} + G_{12}^{ave})} \quad \text{and} \quad |E_2^{III}| \approx \frac{I_0}{2 \text{Im}(G_{22}^{ave} + G_{21}^{ave})} \quad (4.5),$$

where  $G_{\alpha\beta}^{ave} = \frac{G_{\alpha\beta}^I + G_{\alpha\beta}^{III}}{2}$  is the averaged EM coupling at input and output sides. When we compare the transmitted electric field of a non-coupled single rectangular hole  $|E_\alpha^{III}| \approx \frac{I_0}{2 \text{Im}(G_{\alpha\alpha}^{ave})}$ , the above

equations demonstrate clearly that the coupling effect on the

transmission at resonance is governed by the imaginary part of the EM coupling  $G_{\alpha\beta}^{\text{ave}}$ <sup>84</sup>. The interference of the radiated field in the far field region makes the transmission to be effectively enhanced ( $\text{Im}(G_{\alpha\beta}^{\text{ave}}) < 0$ ) or reduced ( $\text{Im}(G_{\alpha\beta}^{\text{ave}}) > 0$ ), depending on the distance between two holes.

#### 4.1.5 Two symmetric THz nano slot antennas

In this chapter, the symmetric coupling in pairs of THz nano slot antennas will be considered as shown in Fig.4.2. The symmetric system consists of two identical rectangular holes with width  $w = 300 \text{ nm}$  and length  $l = 100 \mu\text{m}$ . The fabricated a set of seven samples have different distance  $d$  which is varied from  $200 \mu\text{m}$  down to  $5 \mu\text{m}$ . Notice that the nanometer scale width of the slot antennas enables reaching a few micrometer distance which is a deep subwavelength regime ( $d = 5 \mu\text{m} \sim \lambda_{\text{res}} / 100$  ( $\lambda_{\text{res}} \sim 500 \mu\text{m}$  for the resonance frequency of  $0.6 \text{ THz}$ )). It allows us to realize the strong coupling effect. The left column of Fig. 4.3. presents SEM images of the samples used in the experiment.

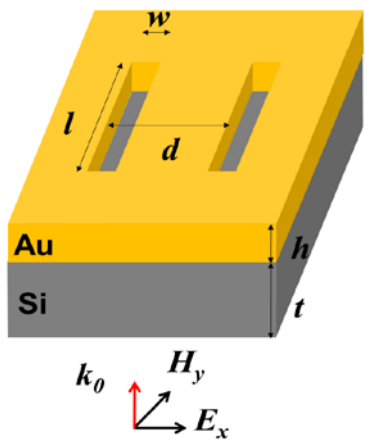


**Fig. 4.2** Geometry of a pair of THz nano slot antennas. The structure consists of two rectangular holes transversely aligned with a various distance  $d$ , perforated on a  $200\text{-nm}$ -thick Au film is deposited on a  $500\text{-}\mu\text{m}$ -thick Si substrate. The two rectangles have the same length ( $l = 100 \mu\text{m}$ ) and the same width ( $w = 300 \text{ nm}$ ), illuminated by horizontally polarized light with normal incidence.

The experimentally acquired transmitted amplitude spectra for these different samples are presented in the middle column of Fig. 4.3. The magnitude of the transmission peak slightly decreases and returns to increase as the distance is reduced from 200  $\mu\text{m}$  to 80  $\mu\text{m}$ . For the sample with the smallest distance ( $d = 5 \mu\text{m}$ ), however, the resonant transmitted amplitude dramatically reduces due to the strong interaction between two nano slot antennas. The calculated total normalized-to-area amplitudes are shown in the right column for a comparison. The discrepancy between the experimental and theoretical calculation can be caused by the calculation based on PEC approximation, as mentioned before. Nevertheless the spectral features and tendencies observed in the experimental results are well reproduced by the theoretical calculations.

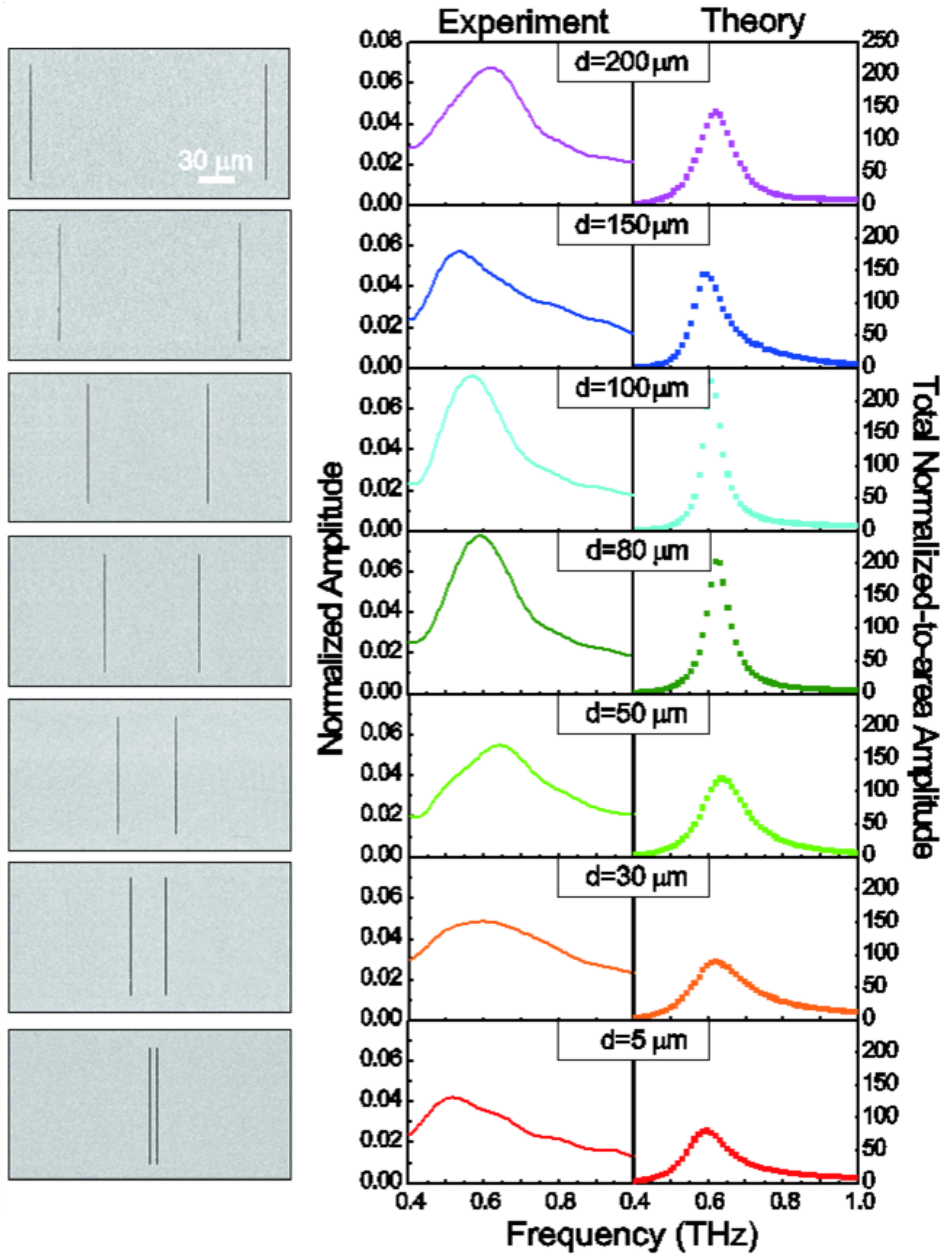


**Fig. 4.3** Experimental and calculated transmission spectra of two symmetric THz nano slot antennas with different distances. SEM images of the corresponding structures are shown in the left column. The middle column shows the measured spectra. The right column shows the calculated total normalized-to-area amplitude for the corresponding  $d$ .

To investigate the evolution of the symmetric coupling behavior, the maximum normalized amplitudes of each sample are divided by that of single nano slot antennas [see Fig. 4.4]. One would expect that the normalized maximum transmission is 2 for two non-coupled slot antennas. A distance-dependent coupling effect is clearly observable when using the normalization: First concentrating on the overall tendency of the maximum transmission, the resonance transmission is not a monotonic function of  $d$ . The origin of the non-monotonic behavior can be traced to the oscillatory and slowly decaying trend of EM coupling,  $\text{Im}(G_{12}^{\text{ave}})$ . Specifically, the total resonant transmission through the pair of rectangles for  $d \sim 100 \mu\text{m}$  is enhanced 3 times more than that of a single hole. It means that the maximum transmission through each hole of the pair increases by a factor 1.5 due to EM coupling ( $\text{Im}(G_{12}^{\text{ave}}) < 0$ ) with respect to that of a single hole. When  $d < 100 \mu\text{m}$ , the transmission is decreasing as  $d$  is reduced and the normalized transmission is smaller than 2 times of single hole case for  $d < 50 \mu\text{m}$  ( $\text{Im}(G_{12}^{\text{ave}}) > 0$ ). This short-range interaction can be understood by the strong overlapping of two large transmission cross-section areas characterizing rectangular holes with extremely large aspect ratio between the length and the width of the rectangle.

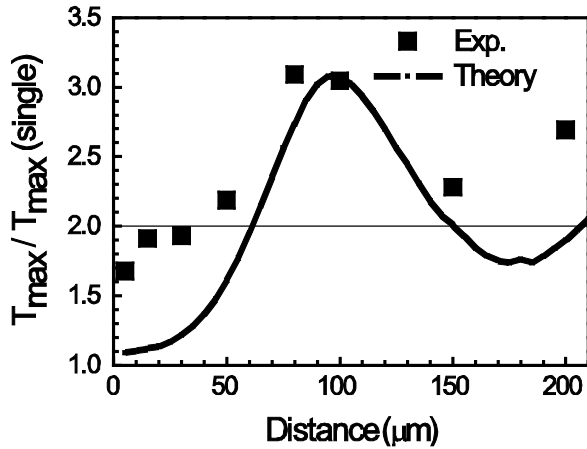


**Fig. 4.4** Evolution of the transmission resonance amplitude normalized by that of a single rectangular hole.

## 4.1.6 Two asymmetric THz nano slot antennas

Next, the transmission properties of asymmetric THz nano slot antenna pairs will be studied as shown in Fig. 4.5. The sample structures consist of two rectangular holes with different lengths,  $l_1 = 150 \mu\text{m}$  and  $l_2 = 100 \mu\text{m}$  but a same width  $w = 350 \text{ nm}$ . The respective resonant frequencies of these rectangles are located at 0.4 THz and 0.6 THz, as demonstrated in Fig. 4.1.3.

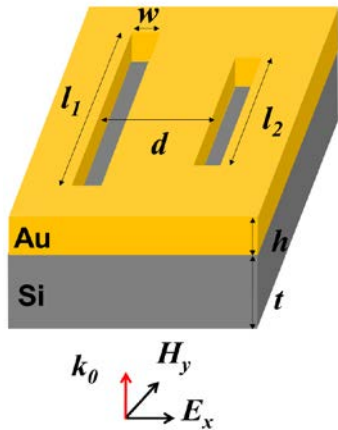


**Fig. 4.5** Geometry of two asymmetric THz nano slot antennas which have different lengths ( $l_1 = 150 \mu\text{m}$  and  $l_2 = 100 \mu\text{m}$ ) and the same width ( $w = 350 \text{ nm}$ ). Two rectangular holes are separated with a various distance  $d$ , and illuminated by horizontally polarized light with normal incidence.

The left column of Fig. 4.6 shows SEM images of different samples with the decreasing  $d$ , from 200  $\mu\text{m}$  down to 2  $\mu\text{m}$ . The measured spectra are shown in the middle column of Fig. 4.6. When the distance between two holes is sufficiently large for weak coupling ( $d = 200 \mu\text{m}$ ), the transmission spectrum shows two well-separated resonances centered at about 0.4 THz (1) and 0.6 THz (2). As the distance is decreased from 200  $\mu\text{m}$ , 170  $\mu\text{m}$  and 130  $\mu\text{m}$ , the only resonance 2 slightly decreases and returns to increase. For  $d = 100 \mu\text{m}$  and 80  $\mu\text{m}$ , it is seen that the resonance 2 is more enhanced while the resonance 1 is slightly reduced, so that the resonance 2 is dominant. By further decreasing  $d$  down to 2  $\mu\text{m}$  which is about 375 and 250 times smaller than two resonance wavelength ( $\lambda_{\text{res}1} \sim 750 \mu\text{m}$  and  $\lambda_{\text{res}2} \sim 500 \mu\text{m}$ ), the resonance 2 is drastically suppressed, and the resonance 1 is more enhanced, resulting in a dominant resonance at 0.4 THz. The strong coupling in the asymmetric system leads to the suppression of higher frequency resonance. As a result, the dominant resonance in the asymmetric system can be modulated and chosen by varying the distance between two nano slot antennas. The modulation nature of the observed results is confirmed by theoretical calculations, which is in good agreement with the experimental results [see the right column of Fig. 4.6].

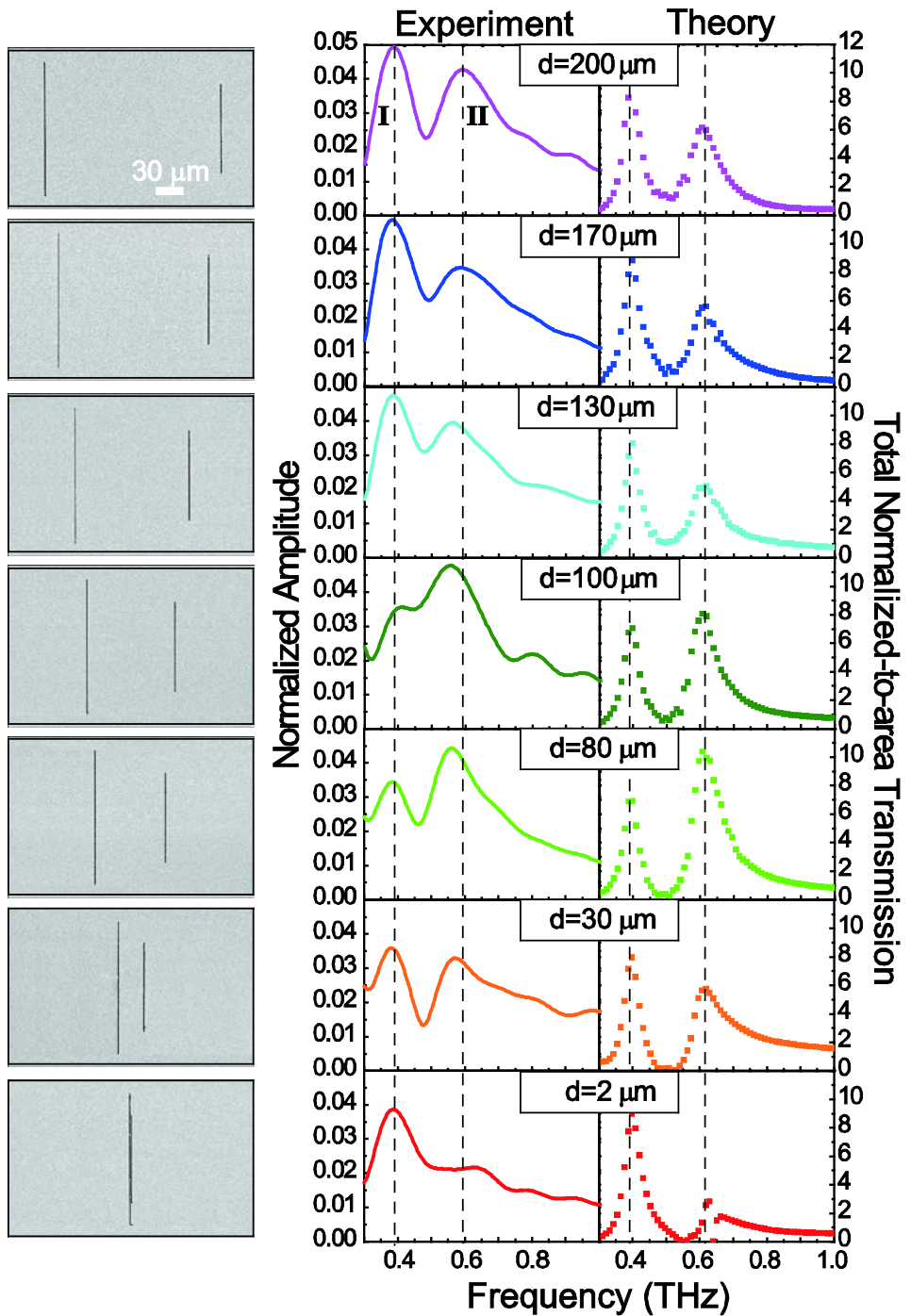


**Fig. 4.6** Transmission spectra for two asymmetric THz nano slot antennas in dependence on the distances  $d$ . SEM images (left column), the measured spectra (middle column), and the theoretical calculations (right column) of the corresponding structures are shown in the figure.

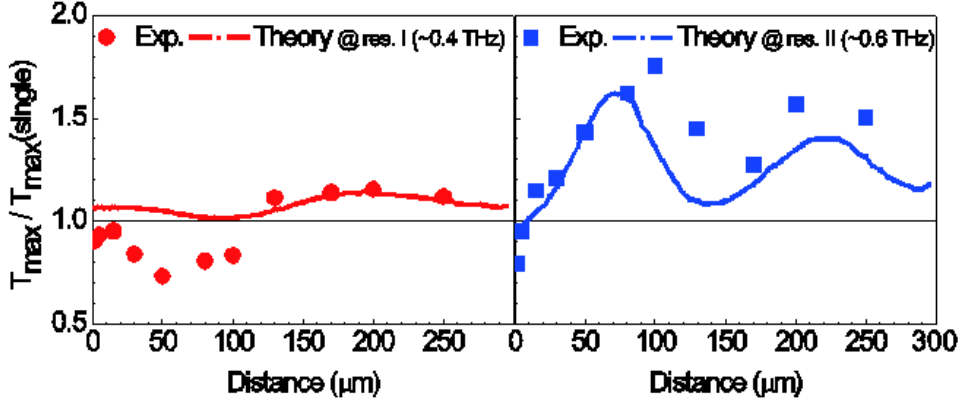


**Fig. 4.7** Evolution of the two resonant transmission normalized by the respective maximum transmission of a single slot antenna as a function of  $d$ .

Figure 4.7 shows the transmission peak at two different resonances normalized by the respective maximum transmission through single holes, as a function of  $d$ . As expected, the maximum transmissions at two resonances have oscillatory behavior as changing the distance. In particular, more enhanced resonance oscillation amplitude at the resonance 2 is clearly observed, while the resonance oscillation amplitude at the resonance 1 is not so much changed. Remarkably, at the resonance 2 the transmitted amplitude reaches up to about two times when compared to the case of single holes. It leads to the change of the dominant resonance from the resonance 1 to the resonance 2. There are two origins of this asymmetric oscillation strength seen in the transmission spectra. One is that the higher frequency resonance can be excited at the longer rectangular hole, while it is difficult to excite the lower frequency resonance at the shorter rectangular hole due to the asymmetric coupling effect. Therefore, the in-phase (out-of-phase) excitation of two rectangular holes can enhance (reduce) the far field transmission of the higher frequency resonance with changing of the distance. The other one is that the oscillating and slowly decaying the coupling effect  $\text{Im}(G_{\alpha\beta}^{\text{ave}})$  which directly influences on the near field enhancement are asymmetric at two different resonance frequencies.

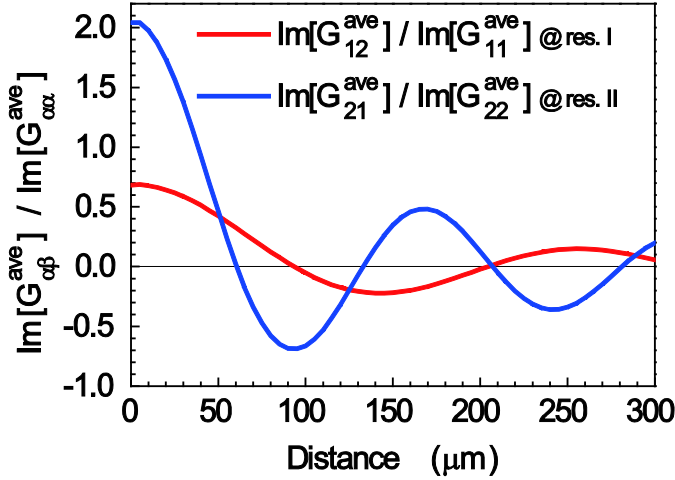


**Fig. 4.8** Evolution of imaginary parts of the averaged EM coupling between two holes,  $G_{\alpha\beta}^{ave} = \frac{G_{\alpha\beta}^I + G_{\alpha\beta}^{III}}{2}$  calculated at resonance 1 and resonance 2.

In Fig 4.8., the EM coupling between two holes  $\text{Im}(G_{\alpha\beta}^{ave})$  normalized by  $\text{Im}(G_{\alpha\alpha}^{ave})$  are plotted as a function of the distance  $d$ . The oscillatory and slowly decaying trend and the period of the coupling terms at two resonances are similar with the change of maximum transmission plotted in Fig. 4.7. As mentioned before, the negative (positive) of  $\text{Im}(G_{\alpha\beta}^{ave})$  is accompanied by the enhanced (suppressed) transmission. In addition, a strong oscillation is observed at resonance 2, while the oscillation at resonance 1 has much weaker amplitude. Particularly, when the distance is decreasing down to the short-range interaction regime,  $\text{Im}(G_{II}^{ave})$  increases up to two times of self-energy of single hole,  $\text{Im}(G_{II}^{ave})$ , which leads to the suppression of the resonance 1. As a results, the asymmetric oscillation strength of the EM coupling leads to the modulation of the dominant resonance peak.

#### 4.1.7 Conclusions

In conclusion, the coupling effects in symmetric and asymmetric terahertz (THz) nano slot antennas pairs have been studied experimentally and theoretically. For the symmetric case, it was found that an optimum distance for the maximum resonant transmission through two coupled rectangular holes exists. In addition, the resonant transmission shows a non-monotonic behavior as increasing the distance between two holes, due to the oscillating and slowly decaying electromagnetic (EM) coupling. By breaking the symmetry of the structure, the oscillation strengths at two different resonances can be modified, showing that the oscillation amplitude at the higher (lower) frequency resonance is enhanced (suppressed). These effects lead to the modulation and interchange of the dominant resonance peak. The nano-sized width of THz slot antennas makes it possible to observe the coupling effect from long-range to short-range. This is because THz nano slot antenna is close to a nano-sized dipole with a large cross-section area, enabling the positioning of the dipole with nanometer resolution and strong interaction. This work provides valuable insight into the design and optimization of rectangular holes with desirable optical properties and functionalities for long wavelength applications.

## 4.2 Array of THz nano slot antennas

### 4.2.1 Introduction

The transmission properties of electromagnetic (EM) waves through periodic sub-wavelength hole arrays have been investigated theoretically and experimentally since Ebbesen found the extraordinary optical transmission phenomenon fifteen years ago<sup>29–32,45</sup>. It has been shown that the resonance transmission properties are influenced by the hole shape and periodicity of the arrays in a wide frequency range from terahertz (THz) to visible light<sup>11,46–58</sup>. For an array of the strongly asymmetric rectangular hole such as THz nano slot antenna compared with square and circular hole, the shape resonance is more dominant than the period effects in the enhanced transmission spectrum<sup>39,79</sup>. As mentioned in the chapter 3.2, this resonant transmission characteristic is mainly determined not only by the length  $l$  but by the width  $w$  of rectangular holes, in which the resonance frequency is close to the cutoff frequency and the electric field inside the hole is critically enhanced as the width decreases<sup>81–83</sup>. Therefore, we can anticipate that the period determines how many apertures effectively interact. One question is how the transmission properties are influenced by strong coupling induced by an extremely close-packed rectangular hole array enabled by the nanoscale width. In this chapter, period effects of the array of THz nano slot antennas will be studied.

## 4.2.2 Array of THz nano slot antennas

We consider various periodic arrays of rectangular holes with a fixed length  $l = 100 \mu\text{m}$  and a width around  $w = 200 \text{ nm}$  perforated on a 100-nm-thick gold (Au) film onto a silicon (Si) substrate as shown schematically in Fig. 4.9(a), where  $d_x$  ( $d_y$ ) is a period of  $x$ - ( $y$ -) direction. The rectangular hole arrays were fabricated with electron-beam lithography and six types of sample with  $d_x = 200 \mu\text{m}$ ,  $150 \mu\text{m}$ ,  $100 \mu\text{m}$ ,  $50 \mu\text{m}$ ,  $20 \mu\text{m}$  and  $2 \mu\text{m}$ , respectively are used. Scanning electron microscope (SEM) images of three samples ( $d_x = 200 \mu\text{m}$ ,  $20 \mu\text{m}$  and  $2 \mu\text{m}$ ) are representatively shown in Fig. 4.9(b). The  $d_y$  is fixed with  $110 \mu\text{m}$ . Notice that the coupling effect along the length side of the rectangular hole can be negligible because the distance between slot antennas along  $y$ -direction is about  $10 \mu\text{m}$  which is much larger than a skin depth of Au in THz frequency regime ( $\sim 100 \text{ nm}$  at 1 THz). The arrangement of THz nano slot antennas along the  $y$ -direction is only for obtaining high signal-to-noise ratio. Because the sample area is limited by the aperture (1 mm by 1 mm), the number of holes depends on the period, ranging from  $N = 5$  holes for the case of  $d_x = 200 \mu\text{m}$  to  $N = 500$  for  $d_x = 2 \mu\text{m}$ .

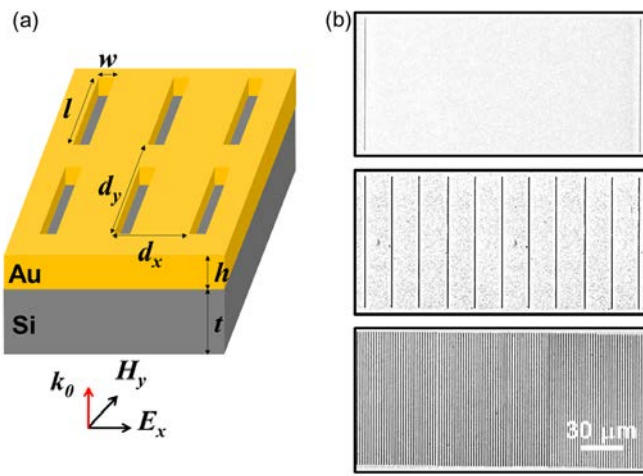


**Fig. 4.9** (a) Schematic of an periodic array of slot antennas. (b) SEM images of array of THz nano slot antennas with different periods,  $d_x = 200 \mu\text{m}$  (top),  $20 \mu\text{m}$  (middle) and  $2 \mu\text{m}$  (bottom).

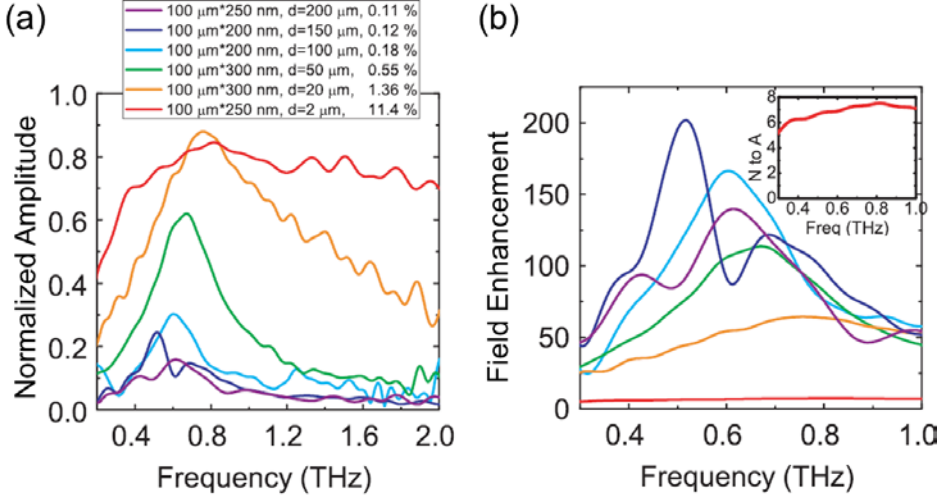


**Fig. 4.10** (a) Normalized transmitted amplitudes with varying the periods from  $d_x = 200 \mu\text{m}$  to  $d_x = 2 \mu\text{m}$ . (b) Corresponding field enhancements as a function of frequencies. The inset of the figure shows the field enhancement of the sample with  $d_x = 2 \mu\text{m}$ .

Figure 4.10(a) renders the normalized amplitudes of transmitted THz waves through the six types of sample with different period  $d_x$ . As clearly shown in this figure, the magnitude of the transmitted amplitude peak increases as  $d_x$  is decreased and  $N$  is increased. For  $d_x = 2 \mu\text{m}$  and  $N = 500$ , the transmission band spans over the whole spectral range from 0.3 to 2 THz, showing over 80% normalized transmission amplitude. Notice that the nanometer scale width of the slot antennas enables reaching a broadband response, which would be impossible using micron-sized widths<sup>39</sup>.

To allow a more direct comparison among the different spectra displayed in Fig 4.10(a) (note that, as mentioned, both  $N$  and  $d_x$  are varied simultaneously from case to case), we have normalized the transmitted electric field amplitude of each sample by the corresponding total area covered by the apertures, corresponding to the field enhancement factor. As seen in Fig. 4.10(b), two important observations emerge when using this normalization. On one hand, both the linewidth and the resonant peak position do not show a monotonic behavior as  $d_x$  is changed.

Specifically, the transmission spectrum for  $d_x = 100 \mu\text{m}$  [see cyan line in Fig. 4.10(b)] has a similar resonant peak position and linewidth to that of a single isolated rectangular hole. When  $d_x = 150 \mu\text{m}$  [blue line in Fig. 4.10(b)], the transmission spectrum shifts to lower frequencies and displays a reduced linewidth. However, for  $d_x = 200 \mu\text{m}$  [violet line in Fig. 4.10(b)], the linewidth is restored and the resonant peak shifts back towards higher frequencies. On the other hand, Fig. 4.10(b) clearly shows how for  $d_x < 100 \mu\text{m}$  the maximum field enhancement severely decreases as  $d_x$  is reduced. This is also an unexpected result: one would expect that the field enhancement at resonance should remain almost constant when  $d_x$  varies for non-coupled system.

### 4.2.3 Theoretical analysis

To understand the physical origin of the observations discussed above, a theoretical coupled-mode formalism based on the modal expansion of the EM fields is applied for array of slot antennas<sup>81,84</sup>. In this calculation, the modeling of the system reduces to solving a system of linear equations for  $E_\alpha^I$  and  $E_\alpha^{III}$  which are the modal amplitudes of the electric field at the input and output sides of the aperture  $\alpha (=1, 2, \dots, N)$ , respectively. Here, the theoretical approach can be simplified by that all the holes in the array behave in the same manner, i.e.,  $E_\alpha^I = E^I$  and  $E_\alpha^{III} = E^{III}$  for all  $\alpha$  in spite of finite number of slot antennas. In this way, the system of linear equations discussed reference 84 transforms into one of only two equations for the modal amplitudes of the central hole (labeled from now on as 0),

$$\begin{aligned} (G^I + S^I - \varepsilon)E - G_v E^{III} &= I \\ (G^{III} + S^{III} - \varepsilon)E^{III} - G_v E &= 0 \end{aligned} \quad (4.6).$$

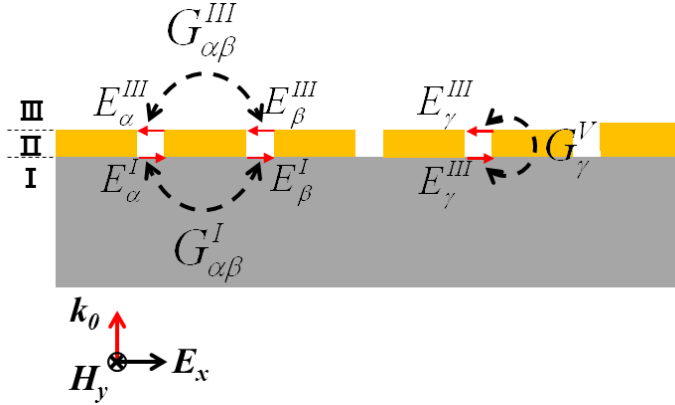


**Fig. 4.11** Schematic cross-sectional view of an array of rectangular holes. The different terms appearing in the equation are also schematically depicted.

The terms  $S^I$  and  $S^{III}$  take into account the *collective re-illumination* process associated with the propagators  $G^I$  and  $G^{III}$  occurring at the two interfaces of the structure. The extremely good accuracy of this approximation is shown in Fig. 4.13 by comparing their results with experimental data.

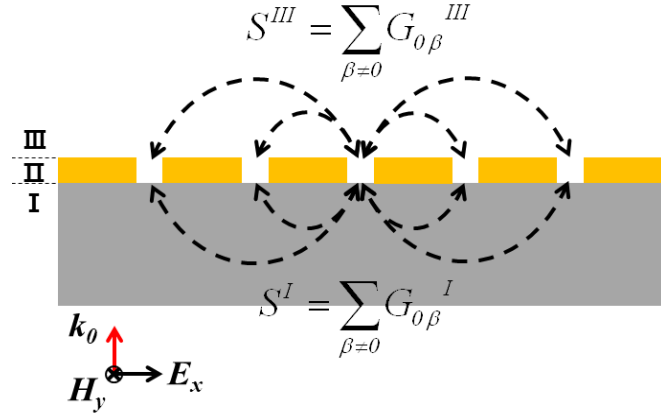


**Fig. 4.12** Schematic of collective re-illumination term  $S^{III}$ .

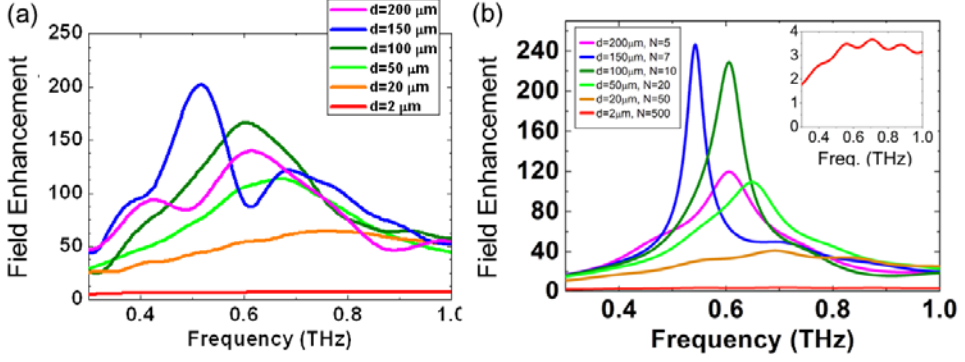


**Fig. 4.13** Experimental data (a) and calculated results (b) of field enhancement for various samples of periodic THz nano slot antenna array.

The crucial point is that the system of two linear equation is formally equivalent to that of a single, isolated rectangular hole<sup>24</sup>. The only difference is that the self-illumination term,  $G^{I,III}$  for a single hole now takes into account the re-illumination coming from other holes by means of  $G^{I,III}+S^{I,III}$ . This mapping shows that  $S^{I,III}$  can be understood as a *self-energy* that sums up the EM coupling of a given hole with all the other holes.

Now we can apply some analytical results found for the case of a single hole to the array of rectangular holes. To further simplify our analytical study, we consider freestanding films with the same geometrical parameters ( $G^I = G^{III} = G$  and  $S^I = S^{III} = S$ ). For example, the spectral location of the resonance is dominantly affected by the real part of  $G+S$  while the normalized to area transmittance at resonance is completely governed by the imaginary part of  $G+S$ <sup>24</sup>. For a single rectangular hole,  $\text{Im}G$  measured the coupling of the fundamental TE mode with radiative modes in vacuum. The presence of other holes and the corresponding interference of their radiated fields in the far-field region make this quantity to be effectively enhanced ( $\text{Im}S > 0$ , constructive interference) or reduced ( $\text{Im}S < 0$  destructive inter), depending on  $d_x$ . Notice that the linewidth of the transmission resonance is also proportional to  $\text{Im}(G+S)$ .

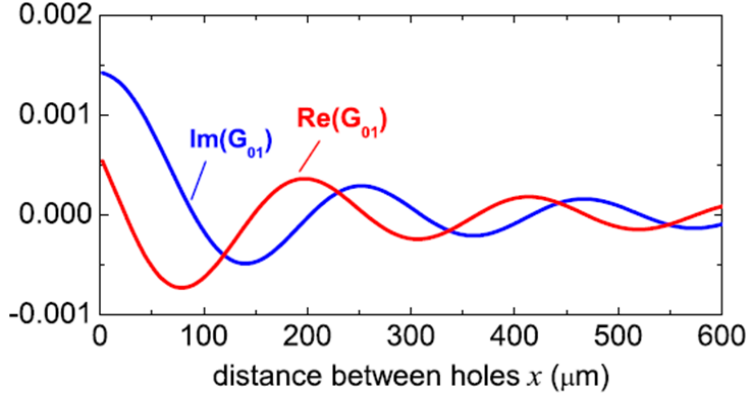


**Fig. 4.14** Imaginary and real parts (shown as blue lines and red lines, respectively) of the EM coupling between two holes,  $G_{01}$ . The two slot antennas labeled with 0 and 1 have same length of  $100\text{ }\mu\text{m}$  and same width of  $200\text{ nm}$  with a distance of  $x$ . We consider freestanding films to simplify the analytical study ( $G_{01}^I = G_{01}^{III} = G_{01}$ ).

The EM coupling between just two holes,  $G_{01}$ , depending on its separation  $d_x$  has an oscillatory (of period  $\lambda$ ) and slow decaying trend, stemming from the behavior of the propagator in real space.

The movement in the spectral location of the transmission resonance can be traced back to the evolution of  $\text{ReS}(d_x)$  as shown in Fig. 4.15. Whenever  $\text{ReS}$  is positive, the resonance shifts to lower frequencies with respect to the resonance location for a single hole, while moving in the opposite direction when  $\text{ReS}$  is negative. Because of the oscillatory behavior of  $\text{Re}(G_{0\beta})$  with  $\beta$ , these shifts are not monotonic functions of  $d_x$ .

Next, we analyze the evolution of  $\text{ImS}(d_x)$ , which governs the peak transmittance and its linewidth, as a function of  $N$ . When  $N$  is small and  $d_x \ll (l, \lambda)$ , we obtain  $\text{Im}G_{0\beta}(\beta d_x \rightarrow 0) \sim \text{Im}G$ . This implies that  $\text{ImS}$  presents a linear scaling with  $N$ ,  $\text{ImS} \sim (N - 1)\text{Im}G$ , as observed in the case  $d_x = 2\text{ }\mu\text{m}$  displayed in Fig. 4.15(b). Correspondingly, as predicted by equation,

$$T_{\text{res}} = \frac{|I_0|^2}{4\text{Im}(G + S)} \quad (4.7),$$

the normalized-to-area transmittance is reduced by a factor  $N$  with respect to that of a single hole and a very broad transmission

spectrum is obtained. Figure 4.15(c) shows maximum of transmittance  $T_{\max}$  as a function of  $N$ . The transmittance  $T_{\max}$  is proportional to  $E_{\max}$ . Therefore, the broadband response also yields to a broadband enhancement of the corresponding electric field.

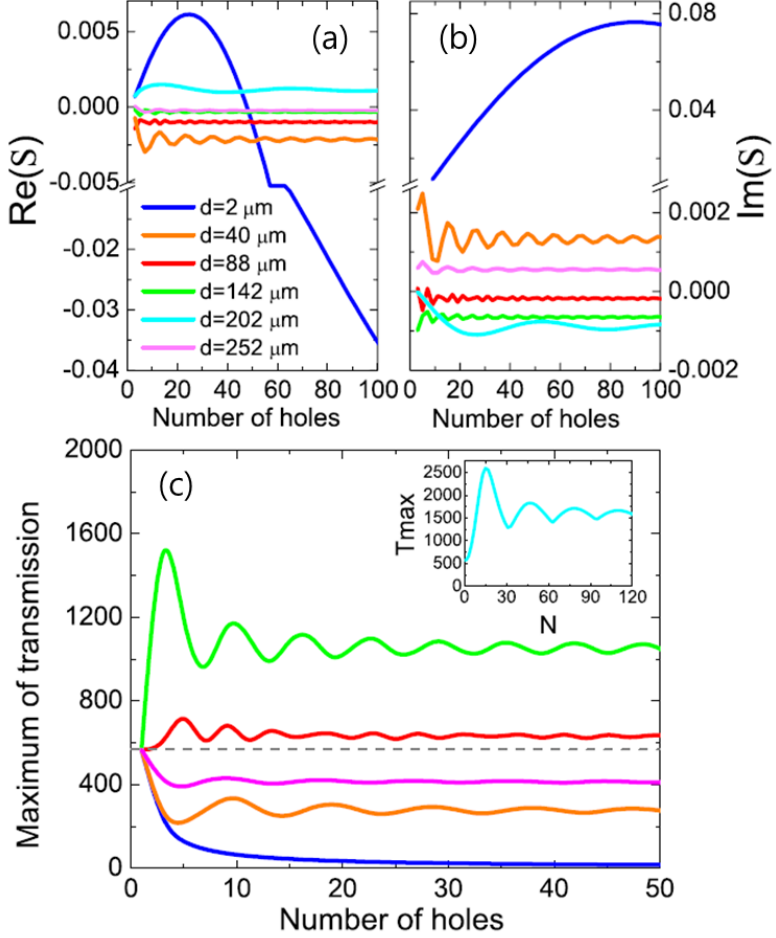


**Fig. 4.15** (a–b) Calculated real and imaginary parts, respectively, of  $S$  versus the number of holes  $N$ . All the magnitudes shown in this figure are evaluated at the resonance frequency of a single hole,  $f_{\text{res}} = 1.43$  THz ( $\lambda_{\text{res}} = 209$  μm). (c) Maximum normalized-to-area transmission  $T_{\max}$  versus the number of apertures computed for the different values of  $d_x$  considered in (a) and (b). Inset displays the case corresponding to  $d_x = 202$  μm. Dashed gray line in main figure corresponds to the value of  $T_{\max}$  for a single isolated hole.

As  $d_x$  is increased but still  $d_x < \lambda / 2$ ,  $\text{Im}G_{0\beta}$  is still positive for the first neighbor interaction, resulting in a short-ranged positive  $\text{Im}S$  [see case  $d_x = 40 \mu\text{m}$  in Fig. 4.15(b)]. As shown in Fig. 4.15(c), this short-range interaction yields to a rapid saturation of  $T_{\max}$  as a function of  $N$ . However, when  $d_x \sim \lambda / 2$  [the case  $d_x = 88 \mu\text{m}$  in Fig. 4.15(b)],  $\text{Im}S$  is close to zero, and therefore  $T_{\max}$  and, consequently, the corresponding linewidth, are very similar to those of a single hole [see Fig. 4.15(b)]. Eventually, for even larger values of  $d_x$ ,  $\text{Im}S$  can be negative ( $d_x = 142 \mu\text{m}$  and  $d_x = 202 \mu\text{m} \sim \lambda$ ), leading to a reduction in their radiative coupling and to an enhanced transmittance at maximum, i.e., to a sharper spectrum. As observed in Fig. 4.15(c), the long-range interhole coupling occurring when  $d_x \sim \lambda$  produces large amplitude oscillations in the evolution of  $T_{\max}$  versus  $N$ . In addition, notice that in this case, huge enhancements of electric field inside the holes are obtained within a very narrow range of frequencies. This narrowing effect occurring at  $d_x \sim \lambda$  has been previously described in arrays of resonators and ascribed either to the formation of lattice resonances<sup>85</sup> or to coherent coupling between the elements<sup>56</sup>. In our case, further increase in  $d_x$  results in  $\text{Im}S$  being positive again, with a slightly reduced transmittance and broader spectrum [see the case  $d_x = 252 \mu\text{m}$  in Figs. 4.15(b) and (c)].

#### 4.2.4 Conclusions

We studied the evolution of the electromagnetic (EM) response with the period of the array of rectangular holes which have a nanoscale width but a length of  $100\text{ }\mu\text{m}$ . We observed band formation in the close-packed terahertz (THz) nano slot antennas. Band formation in covalent solid is mainly determined by the short-range electronic interaction between their constituent atoms. Because of that, when forming a periodic array of  $N$  atoms with period  $d$ , the bandwidth enlarges when  $N$  increases and/or when  $d$  is reduced. Fundamental studies on how this picture is translated into the photonic case are scarce and were done in connection with the emergence of band gaps in dielectric photonic crystals. Here, we realized the photonic band formation with a very elongated rectangular hole perforated on a metal film. The rectangular holes are tailored to work as resonators in the THz frequency regime and can be considered as the constituent atom. Furthermore, it was shown that the EM coupling between THz nano slot antennas forming a periodic array presents a much more complex behavior than the electronic interaction between atoms forming a solid. The EM response with the period is not monotonic due to both the oscillating and slowly decaying EM coupling between holes and its long-range character.

## Chapter 5 Control of field enhancement by geometries of THz nano slits

## 5.1 Introduction

It is important that we investigate the field enhancements for an infinite single slit with non-resonant behavior, where analytical calculations are available, in terms of gaining physical insight and achieving quantitative description of the interaction between millimeter waves with nano-sized aperture<sup>4-10</sup>. In this chapter, an infinitely long single slit on a gold (Au) film is considered. In one previous work reported in 2009, it was shown that an electric field enhancement of 70 nm wide slit at 0.1 THz reached up to 1,000 experimentally. Strikingly, the horizontal electric field is enhanced inside the gap, while the magnetic field is continuously decreasing and spreading inside the metal, with no enhancement in the gap. The origin of the electric field enhancement is that the surface current is induced by the magnetic field of the incident light and the electrical charges are accumulated at the edges of the gap. These charges contribute to the enhancing of the electric field inside the gap<sup>8</sup>. The electric field enhancement strongly depends on the gap size, showing that the field enhancement increases as the gap size decreases. One important topic is what the ultimate limit of the field enhancement will be when the gap size is decreasing, towards one nanometer or below.

## 5.2 Sample fabrication

A few millimeter long single slits can be fabricated with two methods. One is using a focused ion beam (FIB) in which the slits with a few hundred nanometer and a few micrometer sized gap are milled in a row with stitched method. However, the FIB technique gives to us a limit of gap size which depends on not only the ion beam resolution but also a metal thickness because it is difficult to

fabricate the hole with high aspect ratio between metal thickness and gap size. Therefore, we need new fabrication technique for a few nanometer gap perforated on a metal film with a few hundred nanometer thickness. The other one is the technique utilizing photolithography and thin film technology. A single slit with a few nanometer sized gap is fabricated as follows. First, we prepare a patterned 200-nm-thick Au film with a single rectangular structure of 5 mm by 3 mm onto a sapphire substrate using standard photolithography technique. The patterned substrate is then coated with  $\text{Al}_2\text{O}_3$  via atomic layer deposition (ALD) at a typical growth rate of 1–2 Å per cycle. Then, a secondary Au layer is subsequently deposited on the same sample to fill the trench. Finally, an adhesive tape is applied to the surface to peel off the second Au layer selectively. The gap size is controlled by the thickness of  $\text{Al}_2\text{O}_3$  which acts as an insulating layer.

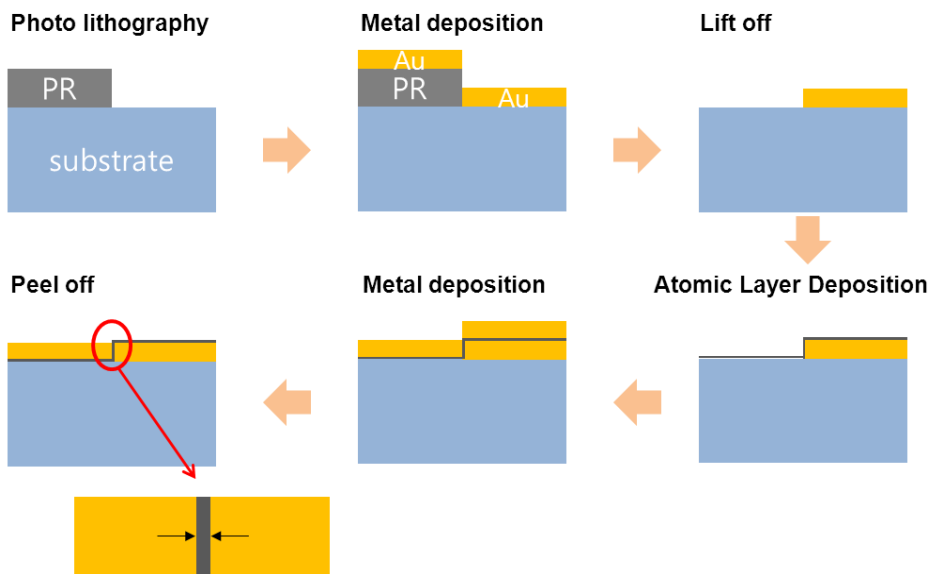


**Fig. 5.1** Atomic layer lithography. A patterned metal film is coated by  $\text{Al}_2\text{O}_3$  using ALD. A secondary metal is deposited on the same sample and an adhesive tape is applied to remove the second metal selectively.

## 5.3 Gap size dependence of field enhancement

In this chapter, the considered structure is an infinite single slit with a various gap size on an Au film deposited on a sapphire substrate (thickness of 650  $\mu\text{m}$ ) as shown in Fig. 5.2. The thickness of Au film ( $h$ ) is 200 nm which is in a skin depth regime ( $\delta_{\text{Au}} \sim 200$  nm at 0.1 THz) and the slit length ( $l$ ) is about 5 mm which can be considered as an infinite length in the sense of being longer than any of the wavelengths used. The gap size ( $w$ ) is decreasing from 50  $\mu\text{m}$  down to 1 nm, covering the aspect ratio  $h / w$  from  $10^{-3}$  up to  $10^2$ .

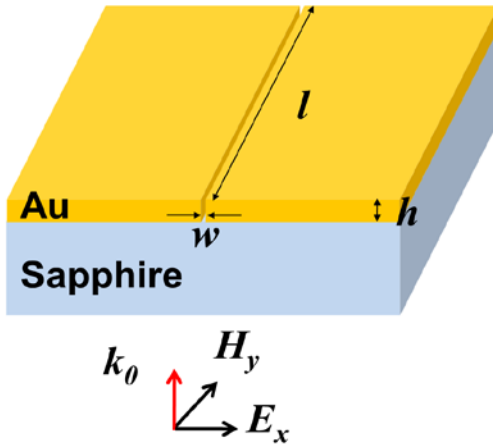


**Fig. 5.2** Schematic of a single slit with a various gap size  $w$  from 50  $\mu\text{m}$  down to 1 nm, on an Au film deposited on a sapphire substrate (thickness of 650  $\mu\text{m}$ ). The thickness of Au film ( $h$ ) is 200 nm which is covering the aspect ratio  $h / w$  from  $10^{-3}$  up to  $10^2$ .

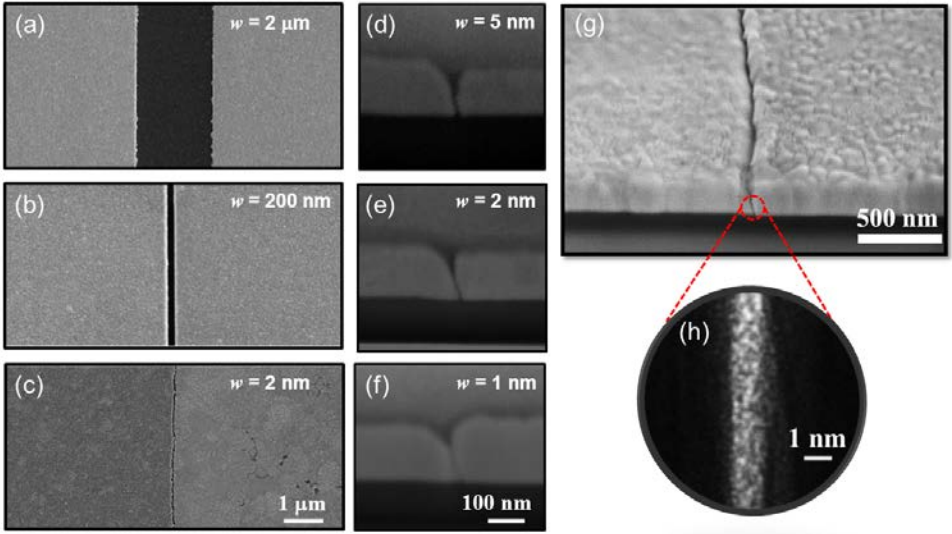


**Fig. 5.3** (a–c) Top view of SEM images for single slits with three different gap sizes ( $w = 2 \mu\text{m}$  (a), 200 nm (b) and 2 nm (c)). (d–f) cross–sectional view of single slits fabricated with atomic layer lithography ( $w = 5 \text{ nm}$  (d), 2 nm (e) and 1 nm(f)). (g–h) Tilted view (g) and TEM image (h) of 1 nm gap.

Figures 5.3(a–c) are top view scanning electron microscope (SEM) images of samples with 2 nm, 200 nm, and 2  $\mu\text{m}$  gap. The samples are made with two methods. One is using a FIB in which the slits with from 200 nm to 50  $\mu\text{m}$  gap are milled in a row with stitched method. The other one is the technique utilizing photolithography and thin film technology as mentioned in the chapter 5.2. With this method, we fabricated the infinite single slits with 1 nm, 2 nm, 5 nm, 10 nm and 20 nm gap filled with  $\text{Al}_2\text{O}_3$  on sapphire substrate. Figures 5.3(d–f) show cross–sectional view SEM images of samples with 5 nm, 2 nm and 1 nm gap, showing the high aspect ratio between the metal thickness ( $h$ ) and the gap size ( $w$ ). As shown in the images, the effective gap thickness of the single slit is about 150 nm when the total metal (Au) thickness is 200 nm. Figure 5.3 (g) is the tilted view SEM image of 1 nm gap sample. The gap size is well defined by the thickness of  $\text{Al}_2\text{O}_3$  layer as shown in the transmission electron microscope (TEM) image [see Figure 5.3(h)].

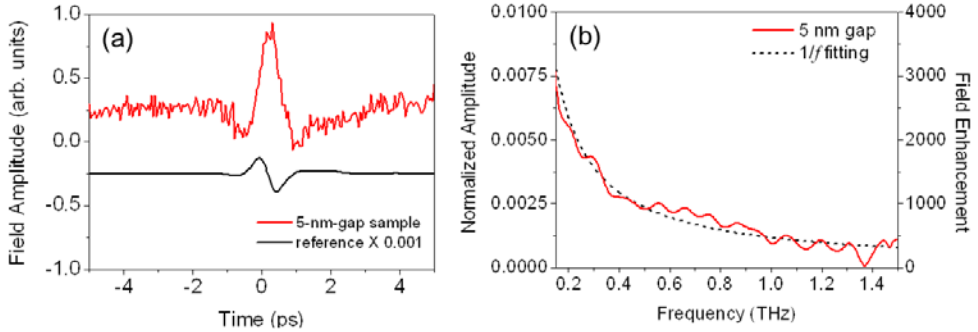


**Fig. 5.4** (a) Time traces of transmitted THz electric field through a single slit with 5 nm gap and bare sapphire for reference. (b) Normalized amplitude and field enhancement of 5 nm gap as a function of frequency. The dotted line indicates a  $1/f$  dependence.

Figure 5.4(a) shows representative time traces of transmitted THz amplitudes through a 5 nm gap sample and a bare quartz substrate with a 1mm by 1 mm aluminum aperture for the  $p$ -polarized incident THz pulses with polarization perpendicular to the slit. The contribution of the direct transmission of the metal film is subtracted. The single cycle pulse shape implies non-resonant behavior and broadband response of the single slit structure. In Fig. 5.4(b), we plotted the normalized transmitted amplitude  $t$  and the electric field enhancement, corresponding to  $t / \beta$  where  $\beta$  is the gap-to-aperture area ratio as explained in the chapter 2. The graph shows that the field enhancement increases with decreasing frequency  $f$ , describing  $1/f$  dependence. This indicates a capacitor-like charging of the gap, because total charge is inversely proportional to the frequency,  $Q_{\text{ind}} \sim I / (i\omega)$  for an alternating current source,  $I = I_0 e^{-i\omega t}$ .

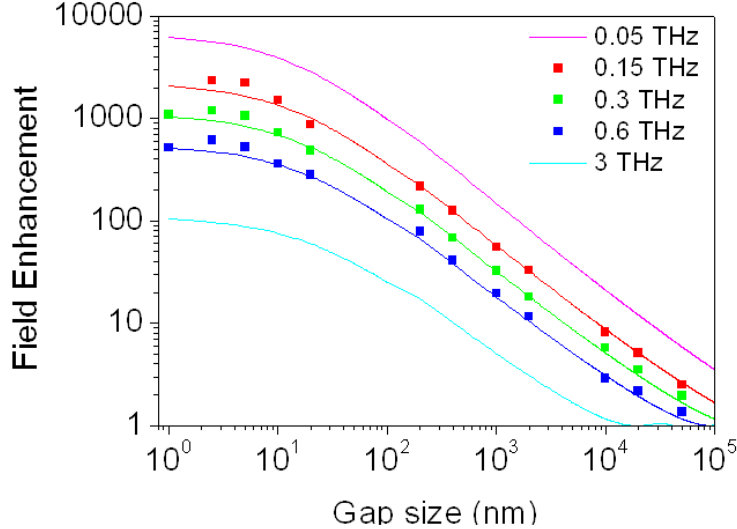
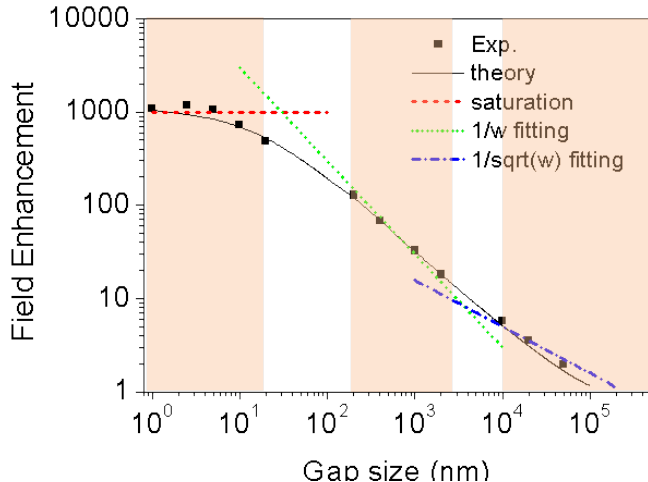


**Fig. 5.5** Field enhancement as a function of gap size at various frequencies. The dotted lines are experimental data and the solid lines are theoretical calculation based on PEC model.

Figure 5.5 renders the electric field enhancement as a function of the gap size with various frequencies. The dot lines are experimental data and the solid lines are theoretical calculation of the modal expansion formalism based on perfect electric conductor (PEC) approximation, which is valid for THz frequency regime. We have checked that both FDTD simulation and PEC modal expansion provided the same results of field enhancement factor. The calculation results are in good agreement with the experimental results. In the figure, we observe two important things. First, the field enhancement increases with decreasing frequency at all gap sizes, indicating a capacitor-like charging of the gap. Second, the field enhancement is increasing as the gap size is decreasing, reaching an ultimate limit with enhancement factor of 2,000 for 1 nm gap at the frequency of 0.15 THz (intensity enhancement of 4 million). This implies reaching a fully capacitive charging regime, realized when  $h / \lambda \ll w / \lambda \ll 1$ . It will be discussed later. The ultimate field enhancement for a given metal thickness is approximately calculated as,

$$FE = \frac{n_{sub} + 1}{2} \frac{\lambda}{\epsilon_d \pi h} \quad (5.1),$$

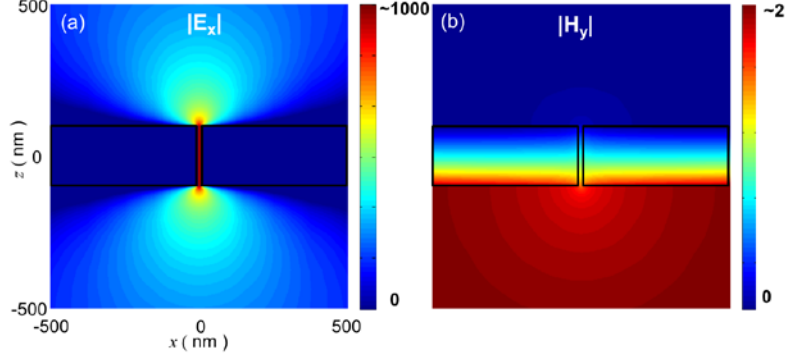
where the  $\epsilon_d$  is dielectric constant of  $\text{Al}_2\text{O}_3$  and  $n_{sub}$  is the refractive index of the sapphire substrate. It provides us a good prediction of the field enhancement with a few thousands. Interestingly, in this regime the field enhancement does not depend on the gap size  $w$  and the metal thickness  $h$  becomes much important parameter. In Fig. 5.6, the field enhancement is monitored continuously from  $w \sim \lambda$  to  $w \ll h$  in order to gain physical insight of an infinite single slit. As we indicate in the figure, three regimes are identified for different values of  $w$ , (1)  $w \sim \lambda$ , (2)  $w \sim h$  ( $\ll \lambda$ ) (3)  $w \ll h$  ( $\ll \lambda$ ). Note again that the metal thickness  $h$  is in a skin depth regime ( $h \sim \delta$ ). The first regime ( $w \sim \lambda$ ) can be explained by two Sommerfeld half plane, showing that the field enhancement increases as  $1/\sqrt{w}$ . For one Sommerfeld half plane, the electric field is proportional to  $1/\sqrt{x}$ , where  $x$  is distance from the edge of the metal plane. When we consider a single slit as two Sommerfeld half plane without coupling, the area normalized electric field is proportional to  $1/\sqrt{w}$ . Accordingly, the field enhancement in this regime is given by  $\sim 1/\sqrt{w}$  dependence. In the regime where  $w \sim h$  ( $\ll \lambda$ ), the field enhancement presents a behavior with  $1/w$ . This is intermediate regime between two Sommerfeld half plane regime and fully capacitive charging regime. Then finally, the third regime arises for  $w \ll h$  ( $\ll \lambda$ ), where the enhancement does not increase, showing the saturated field enhancement. This transition was experimentally observed because we successfully fabricated an infinite single slit with a few nanometer sized gap.



**Fig. 5.6** Field enhancement as a function of gap size at 0.3 THz. The dotted lines distinguish three regimes by fitting the experiment data with different gap size dependence parameter (constant,  $1/w$  and  $1/\sqrt{w}$ ).

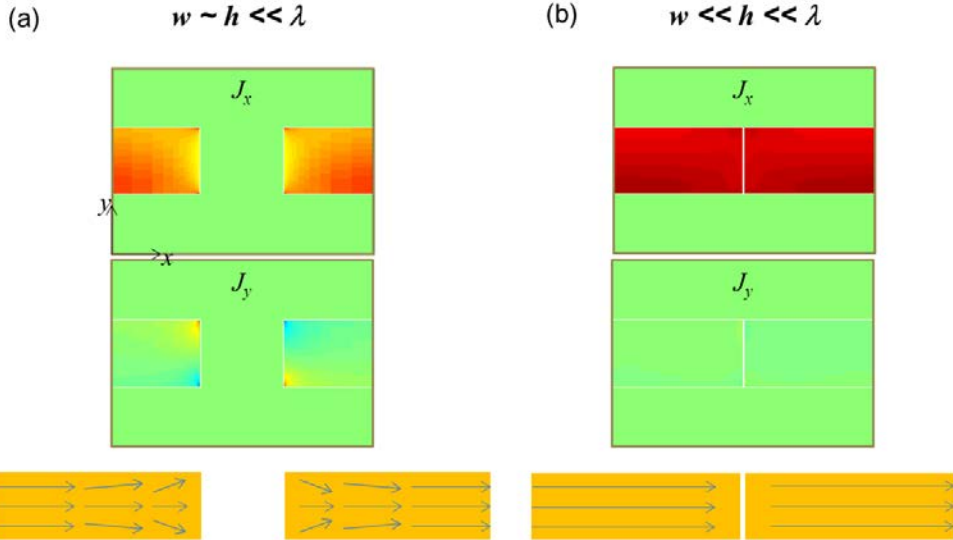
## 5.4 Current and charge distribution of nano slit

To understand the physical origin of saturation phenomena in a few nanometer sized gaps, we have carried out FDTD method simulation. The metal thickness  $h$  is fixed with 200 nm. Figure 5.7(a) and (b) show the electric field distribution and the magnetic field distribution near 1 nm gap, respectively. The electric field is focused in the gap while the magnetic field spread in the metal film without enhancement factor. The electric field enhancement inside gap is determined by the accumulated charge distribution near the gap.



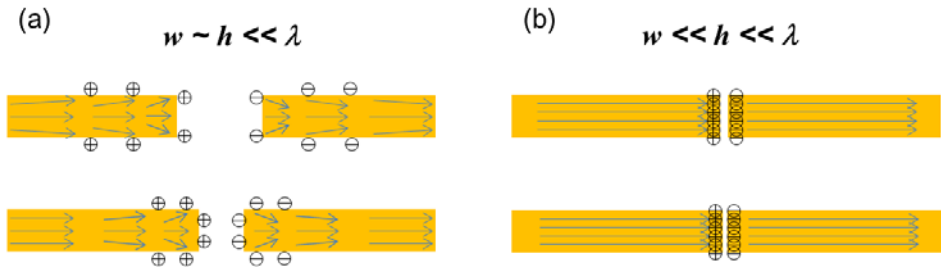
**Fig. 5.7** FDTD simulation of horizontal electric (a) and magnetic (b) field distributions around a nano gap with  $w = 1 \text{ nm}$  and  $h = 200 \text{ nm}$ . The wavelength is 1 mm (0.3 THz).

Figure 5.8(a) and (b) show funneling-induced current density  $\mathbf{J}$  distribution inside the metal film for the gap size of 200 nm and 1 nm, respectively. With two components of current density,  $J_x$  (top) and  $J_y$  (bottom), we schematically show the current distorting near the gap in Fig. 5.8. For  $w = 1 \text{ nm}$ , the current inside the metal film flows straightly whereas the current is more distorted near the gap when  $w = 200 \text{ nm}$ . From the current distribution, we show schematically charge distribution in Fig. 5.8. For  $w = 1 \text{ nm}$ , the electrical charges are mostly accumulated at two edges of the gap whereas the charges are spread in the region of  $x \sim w$  when  $w = 200 \text{ nm}$ .



**Fig. 5.8** FDTD simulation of current distribution inside metal for  $w = 200$  nm (a) and  $w = 1$  nm. (b). The metal (Au) thickness  $h$  is 200 nm.

In the spread charging regime ( $w \sim h$ ), when the gap size is decreased the spread region is decreased thereby the field enhancement inside gap is increased. In the fully capacitive charging regime ( $w \ll h$ ), however, the field enhancement is not changeable because the charge distribution is not changed, leading to the saturation of field enhancement. Therefore, we reached fully capacitive charging-regime with a few nanometer sized gap.



**Fig. 5.9** Schematics of current density and charge distribution near nano gap for spread charging regime (a) and fully capacitive regime (b).

## 5.5 Metal thickness dependence of field enhancement

As mentioned above, the field enhancement is independent on the gap size when we reach a fully capacitive charging-regime ( $w \ll h$ ) realized by a few nanometer sized gap. The saturation point is obtained by equation (5.1). Therefore, in this regime, it is necessary to decrease the thickness of metal film  $h$ . As expected by the equation, the field enhancement again increases when the metal thickness  $h$  decreases. The origin is that the current density  $J$  increases when  $h$  decreases because the surface current  $K$  ( $\sim J \times h$ ) induced by the magnetic field of incident light is constant. In order to verify above description experimentally, we fabricated infinite single slits with 5 nm gap and four different metal thicknesses ( $h = 200$  nm, 150 nm, 70 nm and 50 nm). Figure 5.9 presents the field enhancement of 5 nm gap at 0.3 THz, as a function of the metal thickness. The red line corresponds to the calculated result based on the modal expansion with PEC approximation and the red squares are experimental data which is well matched with the calculation, showing  $1/h$  dependence.

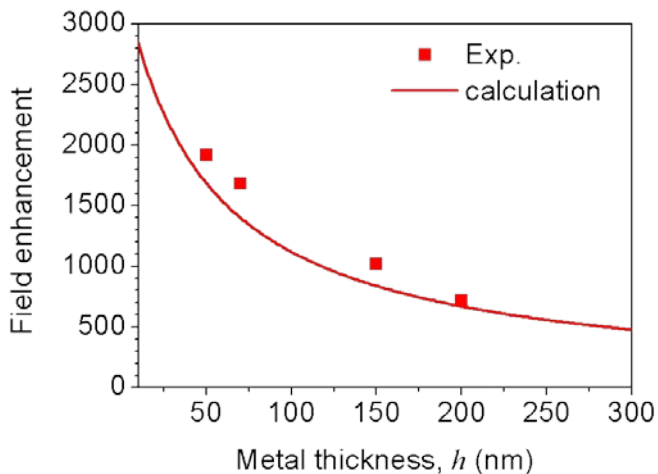


**Fig. 5.10** Field enhancement as a function of metal thickness for 5 nm gap at 0.3 THz. The red line is theoretical calculation based on perfect electric conductor model.

## 5.6 Conclusions

We fabricated an infinite single slit by photolithography and thin film technology. With this method, it is possible to make a few nanometer gap samples, with not only a few millimeter length but also high aspect ratio between metal thickness ( $h$ ), and gap size ( $w$ ). We have reached an ultimate field enhancement of an infinite single slit with high aspect ratio between the metal thickness and the gap size, realized by a few nanometer gap. It can be seen in a fully capacitive charging regime, in which the induced charge resides mostly on the gap surface. Furthermore, this work gives an idea for achieving higher field enhancement in a fully capacitive regime by decreasing the metal thickness.

# Chapter 6 Conclusions

In this thesis, the field enhancement of terahertz (THz) waves in nano gaps, such as nano slot and nano slit, has been investigated both experimentally and theoretically. We have shown that the electric field enhancement of THz nano slot antenna and nano slit was controlled by diverse geometrical parameters, such as gap size, length of the gap, metal thickness and distance between the gaps. The physical origins of the changeable field enhancement were understood by theoretical calculation of the modal expansion formalism based on perfect electric conductor approximation and finite-difference time domain method simulation. We have also introduced standard fabrication procedures, such as focused ion beam, electron-beam lithography and atomic layer lithography, for a nanometer sized patterning in a thin metal film. Using these fabrication techniques, the gap size is controlled from a few hundred nanometer down to one nanometer which is a few million times smaller than the wavelength.

The first part of this thesis deals with coupling effects of THz nano slot antennas which are rectangular holes with a few hundred nanometer width but a length of a few hundred micrometer, tailored to work as resonators in the THz frequency regime. The electromagnetic (EM) interaction between two slots can be controlled by a horizontal distance between the slots because it determines how the transmission cross section areas are overlapped. It was shown that the transmission characteristics including the field enhancement and the resonance peak position present a non-monotonic evolution with the distance due to an oscillating and slowly decaying EM coupling. For the close packed

slot antenna array, it was observed that the transmission band spans over the broad spectral range from 0.2 to 2 THz due to strong coupling between slot antennas. The short-range and long-range EM coupling effects can be observed in the nano-sized width of THz slot antennas because the enhanced field is confined in the nanoscale and the cross section area is a few hundred micronscale. This leads to the positioning of slot antennas with nanometer resolution and the strong coupling strength.

Moreover, we have reached an ultimate limit of THz field enhancement in a single slit with high aspect ratio between the metal thickness and the gap size, realized by a few nanometer gap. The physical origin of the saturation of the field enhancement was investigated through the study of the gap size and the metal thickness effects. In this regime, the induced charge resides mostly at the edges of the nanogap thereby we achieved fully capacitive charging in the nano gap.

Finally, from an applied point of view, these results provide a complete landscape of electric field enhancements attainable in nano structures, which could help in engineering their response. In particular, these results show great promise for a wide spectrum of important applications benefiting from broadband electric field enhancements, such as nonlinear frequency-mixing and sensing devices or thin-film photovoltaics.

## Bibliography

- 1 Chen, X. *et al.* Atomic layer lithography of wafer-scale nanogap arrays for extreme confinement of electromagnetic waves. *Nat Commun* **4**, doi:10.1038/ncomms3361 (2013).
- 2 Seo, M. A. *et al.* Terahertz field enhancement by a metallic nano slit operating beyond the skin-depth limit. *Nat Photon* **3**, 152–156 (2009).
- 3 Im, H., Bantz, K. C., Lindquist, N. C., Haynes, C. L. & Oh, S.-H. Vertically Oriented Sub-10-nm Plasmonic Nanogap Arrays. *Nano Letters* **10**, 2231–2236, doi:10.1021/nl1012085 (2010).
- 4 Ciraci, C. *et al.* Probing the Ultimate Limits of Plasmonic Enhancement. *Science* **337**, 1072–1074, doi:10.1126/science.1224823 (2012).
- 5 Mertens, J. *et al.* Controlling Subnanometer Gaps in Plasmonic Dimers Using Graphene. *Nano Letters* **13**, 5033–5038, doi:10.1021/nl4018463 (2013).
- 6 Kosako, T., Kadoya, Y. & Hofmann, H. F. Directional control of light by a nano-optical Yagi-Uda antenna. *Nat Photon* **4**, 312–315 (2010).
- 7 Kuhn, S., Hakanson, U., Rogobete, L. & Sandoghdar, V. Enhancement of single-molecule fluorescence using a gold nanoparticle as an optical nanoantenna. *Physical Review Letters* **97**, doi:10.1103/PhysRevLett.97.017402 (2006).
- 8 Neubrech, F. *et al.* Resonant Plasmonic and Vibrational Coupling in a Tailored Nanoantenna for Infrared Detection. *Physical Review Letters* **101**, 157403 (2008).
- 9 SchnellM *et al.* Controlling the near-field oscillations of loaded plasmonic nanoantennas. *Nat Photon* **3**, 287–291, doi:[http://www.nature.com/nphoton/journal/v3/n5/supplinfo/nphoton.2009.46\\_S1.html](http://www.nature.com/nphoton/journal/v3/n5/supplinfo/nphoton.2009.46_S1.html) (2009).
- 10 Shegai, T. *et al.* A bimetallic nanoantenna for directional colour routing. *Nat Commun* **2**, 481, doi:[http://www.nature.com/ncomms/journal/v2/n9/supplinfo/ncomms1490\\_S1.html](http://www.nature.com/ncomms/journal/v2/n9/supplinfo/ncomms1490_S1.html) (2011).
- 11 Weber, D. *et al.* Longitudinal and transverse coupling in infrared gold nanoantenna arrays: long range versus short range interaction regimes. *Opt. Express* **19**, 15047–15061 (2011).
- 12 Chen, H.-T. *et al.* Active terahertz metamaterial devices. *Nature* **444**, 597–600, doi:[http://www.nature.com/nature/journal/v444/n7119/supplinfo/nature05343\\_S1.html](http://www.nature.com/nature/journal/v444/n7119/supplinfo/nature05343_S1.html) (2006).
- 13 Liu, M. *et al.* Terahertz-field-induced insulator-to-metal transition in vanadium dioxide metamaterial. *Nature* **487**, 345–348, doi:<http://www.nature.com/nature/journal/v487/n7407/abs/nature11231.html#supplementary-information> (2012).
- 14 Lange, C. *et al.* Extremely nonperturbative nonlinearities in GaAs driven by atomically strong terahertz fields in gold metamaterials. *Physical Review Letters* (2014).

- 15 SchubertO *et al.* Sub-cycle control of terahertz high-harmonic generation by dynamical Bloch oscillations. *Nat Photon* **8**, 119–123, doi:10.1038/nphoton.2013.349 <http://www.nature.com/nphoton/journal/v8/n2/abs/nphoton.2013.349.html#supplementary-information> (2014).
- 16 Huber, R. *et al.* How many-particle interactions develop after ultrafast excitation of an electron-hole plasma. *Nature* **414**, 286–289 (2001).
- 17 Grischkowsky, D., Keiding, S., van Exter, M. & Fattiger, C. Far-infrared time-domain spectroscopy with terahertz beams of dielectrics and semiconductors. *J. Opt. Soc. Am. B* **7**, 2006–2015, doi:10.1364/josab.7.002006 (1990).
- 18 Planken, P. C. M., Nienhuys, H.-K., Bakker, H. J. & Wenckebach, T. Measurement and calculation of the orientation dependence of terahertz pulse detection in ZnTe. *J. Opt. Soc. Am. B* **18**, 313–317, doi:10.1364/josab.18.000313 (2001).
- 19 Wu, Q. & Zhang, X. C. Free-space electro-optic sampling of terahertz beams. *Applied Physics Letters* **67**, 3523–3525, doi:doi:<http://dx.doi.org/10.1063/1.114909> (1995).
- 20 Kyoung, J. S., Seo, M. A., Park, H. R., Ahn, K. J. & Kim, D. S. Far field detection of terahertz near field enhancement of sub-wavelength slits using Kirchhoff integral formalism. *Optics Communications* **283**, 4907–4910, doi:<http://dx.doi.org/10.1016/j.optcom.2010.08.008> (2010).
- 21 Shalaby, M. *et al.* Concurrent field enhancement and high transmission of THz radiation in nanoslit arrays. *Applied Physics Letters* **99**, –, doi:doi:<http://dx.doi.org/10.1063/1.3617476> (2011).
- 22 Bethe, H. A. Theory of Diffraction by Small Holes. *Physical Review* **66**, 163 (1944).
- 23 Roberts, A. Electromagnetic Theory of Diffraction by a Circular Aperture in a Thick, Perfectly Conducting Screen. *J Opt Soc Am A* **4**, 1970–1983 (1987).
- 24 Garc *et al.* Transmission of Light through a Single Rectangular Hole. *Physical Review Letters* **95**, 103901 (2005).
- 25 Webb, K. J. & Li, J. Analysis of transmission through small apertures in conducting films. *Physical Review B* **73**, doi:10.1103/PhysRevB.73.033401 (2006).
- 26 de Abajo, F. J. G. I. Light transmission through a single cylindrical hole in a metallic film. *Opt Express* **10**, 1475–1484 (2002).
- 27 Ebbesen, T. W. *et al.* Beaming light from a subwavelength aperture. *Science* **297**, 820–822, doi:10.1126/science.1071895 (2002).
- 28 Lezec, H. J. *et al.* Beaming Light from a Subwavelength Aperture. *Science* **297**, 820–822 (2002).
- 29 Ebbesen, T. W., Lezec, H. J., Ghaemi, H. F., Thio, T. & Wolff, P. A. Extraordinary optical transmission through sub-wavelength hole arrays. *Nature* **391**, 667–669 (1998).
- 30 Genet, C. & Ebbesen, T. W. Light in tiny holes. *Nature* **445**, 39–46 (2007).

- 31 Vidal, G., Moreno, M., Ebbesen, T. W. & Kuipers, L. Light passing through subwavelength apertures. *Reviews of Modern Physics* **82**, 729–787, doi:citeulike-article-id:6969700 (2010).
- 32 Pendry, J. B., Martín-Moreno, L. & García-Vidal, F. J. Mimicking Surface Plasmons with Structured Surfaces. *Science* **305**, 847–848 (2004).
- 33 Degiron, A., Lezec, H. J., Yamamoto, N. & Ebbesen, T. W. Optical transmission properties of a single subwavelength aperture in a real metal. *Optics Communications* **239**, 61–66, doi:DOI: 10.1016/j.optcom.2004.05.058 (2004).
- 34 Cao, H. & Nahata, A. Resonantly enhanced transmission of terahertz radiation through a periodic array of subwavelength apertures. *Opt. Express* **12**, 1004–1010 (2004).
- 35 Koerkamp, K. J. K., Enoch, S., Segerink, F. B., van Hulst, N. F. & Kuipers, L. Strong Influence of Hole Shape on Extraordinary Transmission through Periodic Arrays of Subwavelength Holes. *Physical Review Letters* **92**, 183901 (2004).
- 36 Gordon, R. *et al.* Strong Polarization in the Optical Transmission through Elliptical Nanohole Arrays. *Physical Review Letters* **92**, 037401 (2004).
- 37 Degiron, A. & Ebbesen, T. W. The role of localized surface plasmon modes in the enhanced transmission of periodic subwavelength apertures. *Journal of Optics A: Pure and Applied Optics* **7**, S90 (2005).
- 38 Ruan, Z. & Qiu, M. Enhanced Transmission through Periodic Arrays of Subwavelength Holes: The Role of Localized Waveguide Resonances. *Physical Review Letters* **96**, 233901 (2006).
- 39 Lee, J. W. *et al.* Terahertz Electromagnetic Wave Transmission through Random Arrays of Single Rectangular Holes and Slits in Thin Metallic Sheets. *Physical Review Letters* **99**, 137401 (2007).
- 40 Lee, J. *et al.* Shape resonance omni-directional terahertz filters with near-unity transmittance. *Opt. Express* **14**, 1253–1259 (2006).
- 41 Bahk, Y. M. *et al.* Anomalous Band Formation in Arrays of Terahertz Nanoresonators. *Physical Review Letters* **106**, 013902 (2011).
- 42 Seo, M. *et al.* Active Terahertz Nanoantennas Based on VO<sub>2</sub> Phase Transition. *Nano Lett* **10**, 2064–2068, doi:10.1021/nl1002153 (2010).
- 43 Kyoung, J. *et al.* Giant nonlinear response of terahertz nanoresonators on VO<sub>2</sub> thin film. *Opt. Express* **18**, 16452–16459 (2010).
- 44 Choi, S. B. *et al.* Nanopattern enabled terahertz all-optical switching on vanadium dioxide thin film. *Applied Physics Letters* **98**, 07105–071103, doi:10.1063/1.3553504 (2011).
- 45 Bravo-Abad, J. *et al.* How light emerges from an illuminated array of subwavelength holes. *Nat Phys* **2**, 120–123 (2006).
- 46 Auguié, B. & Barnes, W. L. Collective Resonances in Gold Nanoparticle Arrays. *Physical Review Letters* **101**, 143902 (2008).
- 47 Liu, N. & Giessen, H. Coupling Effects in Optical Metamaterials. *Angewandte Chemie International Edition* **49**, 9838–9852, doi:10.1002/anie.201003822 (2010).

- 002/anie.200906211 (2010).
- 48 Olk, P., Renger, J., Wenzel, M. T. & Eng, L. M. Distance Dependent Spectral Tuning of Two Coupled Metal Nanoparticles. *Nano Letters* **8**, 1174–1178, doi:10.1021/nl080044m (2008).
- 49 Sersic, I., Frimmer, M., Verhagen, E. & Koenderink, A. F. Electric and Magnetic Dipole Coupling in Near-Infrared Split-Ring Metamaterial Arrays. *Physical Review Letters* **103**, doi:Artn 213902 Doi 10.1103/Physrevlett.103.213902 (2009).
- 50 Kravets, V. G., Schedin, F. & Grigorenko, A. N. Extremely Narrow Plasmon Resonances Based on Diffraction Coupling of Localized Plasmons in Arrays of Metallic Nanoparticles. *Physical Review Letters* **101**, 087403 (2008).
- 51 Taubert, R., Ameling, R., Weiss, T., Christ, A. & Giessen, H. From Near-Field to Far-Field Coupling in the Third Dimension: Retarded Interaction of Particle Plasmons. *Nano Letters* **11**, 4421–4424, doi:Doi 10.1021/Nl202606g (2011).
- 52 Artar, A., Yanik, A. A. & Altug, H. Multispectral Plasmon Induced Transparency in Coupled Meta-Atoms. *Nano Letters*, null-null, doi:10.1021/nl200197j (2011).
- 53 Halas, N. J., Lal, S., Chang, W.-S., Link, S. & Nordlander, P. Plasmons in Strongly Coupled Metallic Nanostructures. *Chemical Reviews* **111**, 3913–3961, doi:10.1021/cr200061k (2011).
- 54 Kim, D. S. *et al.* Real-Space Mapping of the Strongly Coupled Plasmons of Nanoparticle Dimers. *Nano Letters* **9**, 3619–3625, doi:Doi 10.1021/Nl901839f (2009).
- 55 Fischer, H. & Martin, O. J. F. Retardation-induced plasmonic blinking in coupled nanoparticles. *Opt. Lett.* **34**, 368–370 (2009).
- 56 Fedotov, V. A. *et al.* Spectral Collapse in Ensembles of Metamolecules. *Physical Review Letters* **104**, 223901 (2010).
- 57 Xu, H. *et al.* Tight-binding analysis of coupling effects in metamaterials. *Journal of Applied Physics* **109**, 023103–023108, doi:10.1063/1.3533948 (2011).
- 58 Hentschel, M. *et al.* Transition from Isolated to Collective Modes in Plasmonic Oligomers. *Nano Letters* **10**, 2721–2726, doi:10.1021/nl101938p (2010).
- 59 Yang, Z.-J. *et al.* Fano resonances in dipole-quadrupole plasmon coupling nanorod dimers. *Opt. Lett.* **36**, 1542–1544 (2011).
- 60 Wu, C. *et al.* Fano-resonant asymmetric metamaterials for ultrasensitive spectroscopy and identification of molecular monolayers. *Nat Mater* **11**, 69–75 (2012).
- 61 Singh, R. *et al.* Observing metamaterial induced transparency in individual Fano resonators with broken symmetry. *Applied Physics Letters* **99**, 201107–201103, doi:10.1063/1.3659494 (2011).
- 62 Singh, R., Al-Naib, I. A. I., Koch, M. & Zhang, W. Sharp Fano resonances in THz metamaterials. *Opt. Express* **19**, 6312–6319 (2011).
- 63 Sheikholeslami, S., Jun, Y.-w., Jain, P. K. & Alivisatos, A. P. Coupling of Optical Resonances in a Compositionally Asymmetric Plas

- monic Nanoparticle Dimer. *Nano Letters* **10**, 2655–2660, doi:10.1021/nl101380f (2010).
- 64 Rahmani, M. *et al.* Influence of symmetry breaking in pentamers  
on Fano resonance and near-field energy localization. *Opt. Mater. Express* **1**, 1409–1415 (2011).
- 65 Peña-Rodríguez, O. *et al.* Enhanced Fano Resonance in Asymmetrical Au:Ag Heterodimers. *The Journal of Physical Chemistry C* **115**, 6410–6414, doi:10.1021/jp200495x (2011).
- 66 Luk'yanchuk, B. *et al.* The Fano resonance in plasmonic nanostructures and metamaterials. *Nat Mater* **9**, 707–715 (2010).
- 67 Liu, Z. F. & Jin, G. J. Phase effects in the enhanced transmission through compound subwavelength rectangular hole arrays. *Journal of Applied Physics* **106**, doi:Artn 063122 Doi 10.1063/1.3225906 (2009).
- 68 Lassiter, J. B. *et al.* Fano Resonances in Plasmonic Nanoclusters: Geometrical and Chemical Tunability. *Nano Letters* **10**, 3184–3189, doi:10.1021/nl102108u (2010).
- 69 Hendry, E., Mikhaylovskiy, R. V., Barron, L. D., Kadodwala, M. & Davis, T. J. Chiral Electromagnetic Fields Generated by Arrays of Nanoslits. *Nano Letters*, doi:10.1021/nl3012787 (2012).
- 70 Fedotov, V. A. *et al.* Temperature control of Fano resonances and transmission in superconducting metamaterials. *Opt. Express* **18**, 9015–9019 (2010).
- 71 Fedotov, V. A., Rose, M., Prosvirnin, S. L., Papasimakis, N. & Zheludev, N. I. Sharp Trapped-Mode Resonances in Planar Metamaterials with a Broken Structural Symmetry. *Physical Review Letters* **99**, 147401 (2007).
- 72 Encina, E. R. & Coronado, E. A. On the Far Field Optical Properties of Ag–Au Nanosphere Pairs. *The Journal of Physical Chemistry C* **114**, 16278–16284, doi:10.1021/jp105522b (2010).
- 73 Christ, A., Martin, O. J. F., Ekinci, Y., Gippius, N. A. & Tikhodeev, S. G. Symmetry Breaking in a Plasmonic Metamaterial at Optical Wavelength. *Nano Letters* **8**, 2171–2175, doi:10.1021/nl0805559 (2008).
- 74 Christ, A. *et al.* Controlling the Fano interference in a plasmonic lattice. *Physical Review B* **76**, 201405 (2007).
- 75 Chen, C.-Y., Un, I.-W., Tai, N.-H. & Yen, T.-J. Asymmetric coupling between subradiant and superradiant plasmonic resonances and its enhanced sensing performance. *Opt. Express* **17**, 15372–15380 (2009).
- 76 Bachelier, G. *et al.* Fano Profiles Induced by Near-Field Coupling in Heterogeneous Dimers of Gold and Silver Nanoparticles. *Physical Review Letters* **101**, 197401 (2008).
- 77 Kang, J. H., Choe, J.-H., Kim, D. S. & Park, Q. H. Substrate effect on aperture resonances in a thin metal film. *Opt. Express* **17**, 15652–15658 (2009).
- 78 Park, H. R. *et al.* Resonance behavior of single ultrathin slot antennas on finite dielectric substrates in terahertz regime. *Applied P*

- 79 *physics Letters* **96**, 211109–211103, doi:10.1063/1.3437091 (2010).  
Park, H. R. *et al.* Terahertz nanoresonators: Giant field enhancement and ultrabroadband performance. *Applied Physics Letters* **96**, 121106–121103, doi:10.1063/1.3368690 (2010).

80 Jeong, Y.-G. *et al.* Electrical control of terahertz nano antennas on VO<sub>2</sub> thin film. *Opt. Express* **19**, 21211–21215 (2011).

81 García-Vidal, F. J., Moreno, E., Porto, J. A. & Martín-Moreno, L. Transmission of Light through a Single Rectangular Hole. *Physical Review Letters* **95**, 103901 (2005).

82 Seo, M. A. *et al.* Near field imaging of terahertz focusing onto rectangular apertures. *Opt. Express* **16**, 20484–20489 (2008).

83 García-Vidal, F. J., Martín-Moreno, L., Moreno, E., Kumar, L. K. S. & Gordon, R. Transmission of light through a single rectangular hole in a real metal. *Physical Review B* **74**, 153411 (2006).

84 Garcia-Vidal, F. J., Martin-Moreno, L., Ebbesen, T. W. & Kuipers, L. Light passing through subwavelength apertures. *Reviews of Modern Physics* **82**, 729–787 (2010).

85 Vecchi, G., Giannini, V., & mez Rivas, J. Shaping the Fluorescent Emission by Lattice Resonances in Plasmonic Crystals of Nanoantennas. *Physical Review Letters* **102**, 146807 (2009).

## 요약(국문초록)

본 논문에서는 나노 슬릿 안테나 혹은 나노 슬릿의 구조에 따른 테라헤르츠 전기장 집속율 변화를 탐구하였다. 나노 캡의 사이즈는 수 백 나노미터부터 1 나노미터까지 다양하게 제작하였으며 이는 파장보다 1,000 배부터 1,000,000 배까지 작은 구멍을 구현한 것으로 볼 수 있다. 길이가 수 백 마이크로미터이고 폭이 수 백 나노미터인 나노 슬릿 안테나의 경우 테라헤르츠 주파수 대역에서 강한 투과 공명 현상이 일어나는데 이는 테라파의 전기장이 캡에 강하게 집속되기 때문이다. 이때 공명 주파수는 주로 직사각형 구멍의 길이에 의해 정해지며 집속율은 직사각형 폭이 줄어들수록 증가한다. 본 논문에서는 이러한 나노 슬릿 안테나를 폭 방향으로 나란히 정렬하고 슬릿 안테나 사이의 거리를 변화시켜 슬릿 안테나 사이의 전자기학적 상호작용에 따른 테라파 전기장 집속율의 변화를 탐구하였다. 여기서 슬릿 안테나 사이의 거리는 파장보다 수 백배 작은 2 마이크로미터까지 줄일 수 있는데 이를 통해 슬릿 안테나 사이의 강한 상호작용을 구현할 수 있다. 강한 상호 작용의 효과로 나노 슬릿 안테나가 넓은 테라헤르츠 주파수 영역대에서 반응함을 관측하였고 이는 마이크로미터 캡을 지닌 슬릿 안테나에서는 볼 수 없는 새로운 현상이다. 또한 슬릿 안테나 사이의 전자기학적 상호작용이 거리에 따라 진동하며 감쇠하는 성질을 이용하여 슬릿 안테나의 공명 주파수와 전기장 집속율을 자유롭게 변화시킬 수 있다. 한편, 나노 슬릿은 일차원 구조로써 나노캡에서 테라파가 어떻게 투과하는지를 살펴보기 가장 좋은 구조라고 할 수 있다. 본 논문에서는 수 밀리미터 길이와 수 나노미터 캡 크기를 가진 나노 슬릿을 제작하여 캡 크기가 파장보다 1,000,000 배 작은 구조를 구현하였다. 나노 캡에 테라파를 입사시켜 전기장 집속율을 측정한 결과, 캡 크기가 수십 마이크로미터에서 수십 나노미터로 줄어들 때 테라헤르츠 전기장 집속율은 점점 증가하다가 수 나노미터까지 줄어들면 집속율이 더 이상 증가하지 않고 일정하게 유지되는 것을

실험을 통해 확인하였다. 테라파의 전기장 집속 현상은 입사하는 테라파의 자기장에 의해 유도된 표면 전류로 인해 캡 주변에 전하가 모이면서 일어나는데, 이때 유도되는 전하의 총량은 입사하는 빛의 자기장에 의해 결정되므로 구조에 따라 변하지 않는다. 하지만 캡 크기가 줄어들수록 유도된 전하는 캡 가까이에 모이게 되어 단위 면적 당 전하량이 증가하여 전기장 집속율이 증가하게 된다. 따라서 전기장의 집속율이 더 이상 변하지 않는 것은 캡 가장자리에 대부분의 전하가 모여있는 것을 의미하고 이는 전기장 집속율의 극한 값에 도달하였음을 의미한다. 이러한 나노 캡의 구조에 따른 테라파의 전기장 증폭율 변화에 대한 연구는 나노미터 구멍에서 빛이 투과하는 현상을 물리적으로 깊이 이해하는데 도움이 될 뿐만 아니라 나노미터 스케일의 광학 소자 개발 및 응용에 활용될 수 있을 것이다.

주요어: 테라헤르츠 시분할 분광; 테라헤르츠 플라즈모닉스; 파장보다 작은 구조; 나노캡; 전기장 집속율; 상호작용;

학번: 2004-20430

## List of publications

1. Young-Mi Bahk, Gopakumar Ramakrishnan, Jongho Choi, Hyelynn Song, Geunchang Choi, Yong Hyup Kim, Kwang Jun Ahn, Dai-Sik Kim, and Paul C. M. Planken, “*Plasmon enhanced terahertz emission from single layer graphene,*” *ACS Nano* **8**, 9089 (2014).
2. Hyeong-Ryeol Park, Kwang Jun Ahn, Sanghoon Han, Young-Mi Bahk, Namkyoo Park, and Dai-Sik Kim, “*Colossal absorption of molecules inside single terahertz nanoantennas,*” *Nano Letters* **13(4)**, 1782 (2013).
3. (Book chapter) “Fundamental aspects of terahertz near-field imaging and sensing”, D. S. Kim, Y. M. Bahk and P. C. M. Planken, Handbook of terahertz technology for imaging, sensing and communications, Book edited by Daryoosh Saeedkia, ISBN: 978-0-85709-235-9, Publisher: Woodhead Publishing (2013).
4. Young-Mi Bahk (corresponding author), Jae-Wook Choi, Jisoo Kyoung, Hyeong-Ryeol Park, Kwang Jun Ahn, and Dai-Sik Kim, “*Selective enhanced resonances of two asymmetric terahertz nano resonators,*” *Optics Express* **20(23)**, 25644 (2012).
5. Y. M. Bahk, H. R. Park, K. J. Ahn, H. S. Kim, Y. H. Ahn, Dai-

- Sik Kim, J. Bravo-Abad, L. Martin-Moreno, and F. J. Garcia-Vidal, “*Anomalous band formation in arrays of terahertz nanoresonators*,” *Physics Review Letters* **106**, 013902 (2011).
6. Hyeong-Ryeol Park, Young-Mi Bahk, Jong Ho Choe, Sanghoon Han, Seong Soo Choi, Kwang Jun Ahn, Namkyoo Park, Q-Han Park, and Dai-Sik Kim, “*Terahertz pinch harmonics enabled by single nano rods*,” *Optics Express* **19**, 24775 (2011).
  7. Hyeong-Ryeol Park, Young-Mi Bahk, Kwang Jun Ahn, Q-Han Park, Dai-Sik Kim, Luis Martin-Moreno, Francisco J. Garcia-Vidal, and Jorge Bravo-Abad, “*Controlling terahertz radiation with nanoscale metal barriers embedded in nano slot antennas*,” *ACS Nano* **5**, 8340 (2011).
  8. H. R. Park, Y. M. Park, H. S. Kim, J. S. Kyoung, M. A. Seo, D. J. Park, Y. H. Ahn, K. J. Ahn, and D. S. Kim, “*Terahertz nano-resonators: giant field enhancement and ultrabroadband performance*,” *Applied Physics Letters* **96**, 121106 (2010).
  9. Jisoo Kyoung, Minah Seo, Hyeongryeol Park, Sukmo Koo, Hyun-sun Kim, Youngmi Park, Bong-Jun Kim, Kwangjun Ahn, Namkyoo Park, Hyun-Tak Kim, and Dai-Sik Kim, “*Giant nonlinear response of terahertz nanoresonators on VO<sub>2</sub> thin film*,” *Optics Express* **18**, 16452 (2010).
  10. H. R. Park, S. M. Koo, O. K. Suwal, Y. M. Park, J. S. Kyoung, M. A. Seo, S. S. Choi, N. K. Park, D. S. Kim and K. J. Ahn, “*Resonance behavior of single ultrathin slot antennas on finite dielectric substrates in terahertz regime*,” *Applied Physics Letters* **96**, 211109 (2010).

## Conferences

1. J.-Y. Kim, B. J. Kang, W. T. Kim, J. Park, J. Rhie, Y. M. Bahk, T. Kang, H. Jeon, F. Rotermund, and D. S. Kim “*Self-limiting dielectric response in nanogaps from high-field terahertz,*” KPS 2014, Gwangju, Korea, 22–24 October, 2014.
2. J. Jeong, J. Rhie, Y. M. Bahk, and D. S. Kim “*Terahertz wave transmission through 10 nm gap array,*” KPS 2014, Gwangju, Korea, 22–24 October, 2014.
3. K. Lee, J. Rhie, Y. M. Bahk, J. Jeong, and D. S. Kim “*Huge field enhancement in microwave range achieved by  $\lambda/2,000$ -width antennas,*” IRMMW–THz 2014, Tucson, AZ, USA, 14–19 September, 2014.
4. J. S. Ahn, T. Kang, D. K. Singh, Y. M. Bahk, J. Kim, J. Rhie, J. Jeong, and D. S. Kim “*Optical field enhancement of one nanometer gaps at near infrared frequencies,*” Near Field Optics 13, Salt Lake City, USA, 31 August –4, September, 2014.
5. D. Lee, Y. M. Bahk, S. Han, J. Rhie, J. S. Ahn, and D. S. Kim “*Optical magnetic scattering from single rectangular holes,*” Photonics West 2014, San Francisco, USA, 1–6 February, 2014.
6. J. Rhie, H. R. Park, Y. M. Bahk, and D. S. Kim “*Strong absorption of molecules inside terahertz nano-slot antenna,*” Photonics West 2014, San Francisco, USA, 1–6 February, 2014.
7. Y. M. Bahk, J. Rhie, D. S. Kim “*Funneling of millimeter waves*

- through 5-nm gap,”* Photonics West 2014, San Francisco, USA, 1–6 February, 2014.
8. S. Han, Y. M. Bahk, N. K. Park, and D. S. Kim “*10,000-fold field enhancement for millimeter-wave transmission through one-nanometer gaps,*” Photonics West 2014, San Francisco, USA, 1–6 February, 2014.
  9. S. Han, Y. M. Bahk, N. K. Park, and D. S. Kim “*Electric field enhancement tendency of nanometer slit structure at terahertz regime,*” KPS 2013, Changwon, Korea, 30–31 October, 1 November, 2013.
  10. T. Kang, Y. M. Bahk, W. Park, and D. S. Kim “*Interferometric measurement of field enhancements in one nanometer gaps,*” KPS 2013, Changwon, Korea, 30–31 October, 1 November, 2013.
  11. D. Lee, Y. M. Bahk, J. Rhie, J. S. Ahn, S. Han, and D. S. Kim “*Optical magnetic scattering from single rectangular holes,*” Optical Society of Korea Summer Meeting 2013, Yeosu, Korea, 10–12 July, 2013.
  12. K. Lee, Y. M. Bahk, J. Jeong, and D. S. Kim “*Resonance properties of asymmetric slot antenna pairs in deep subwavelength regime,*” Optical Society of Korea Summer Meeting 2013, Yeosu, Korea, 10–12 July, 2013.
  13. Y. M. Bahk, J. Rhie, H. R. Park, J. Jeong, and D. S. Kim “*Funneling of terahertz waves through  $\lambda/1,000,000$  nanogap,*” Optical Society of Korea Summer Meeting 2013, Yeosu, Korea, 10–12 July, 2013.
  14. J. Rhie, H. R. Park, Y. M. Bahk, G. Choi, and D. S. Kim “*Strong absorption of lactose molecule inside terahertz nano-slot antenna,*” Optical Society of Korea Summer Meeting 2013, Yeosu, Korea, 10–12 July, 2013.
  15. Y. M. Bahk, G. Ramakrishnan, J. H. Choi, H. R. Park, K. J. Ahn, Y. H. Kim, P. C. M. Planken, and D. S. Kim “*Surface plasmon-enhanced terahertz emission from single layer*

- graphene,”* SPP6 (The 6<sup>th</sup> International Conference of Surface Plasmon Photonics), Ottawa, Canada, 26–31 May, 2013.
16. H. R. Park, K. J. Ahn, S. Han, Y. M. Bahk, N. K. Park, and D. S. Kim “*Colossal absorption of molecules inside single terahertz nano-slot antennas,*” SPP6 (The 6<sup>th</sup> International Conference of Surface Plasmon Photonics), Ottawa, Canada, 26–31 May, 2013.
17. K. H. Lee, Y. M. Bahk, and D. S. Kim “*Experimental study of microwave resonances for  $\lambda/400$  slot antennas,*” KPS 2013, Daejeon, Korea, 24–26 April, 2013.
18. D. Lee, Y. M. Bahk, S. Han, J. Rhie, J. S. Ahn, and D. S. Kim “*Magnetic scattering of light from a single rectangular hole,*” KPS 2013, Daejeon, Korea, 24–26 April, 2013.
19. K. H. Lee, Y. M. Bahk, and D. S. Kim “*Experimental study of microwave resonances for  $\lambda/400$  slot antennas,*” Asia-Pacific Microwave Photonics Conference 2013, Gwangju, Korea, 22–24 April, 2013.
20. H. R. Park, Y. M. Bahk, K. J. Ahn, and D. S. Kim “*Terahertz nano antennas for sensing and tuning,*” FTT 2012, Nara, Japan, 26–30 November, 2012.
21. Y. M. Bahk, H. R. Park, K. Lee, D. Lee, D. S. Kim, G. Ramakrishnan, P. C. M. Planken, J. H. Choi, T. J. Kang, and Y. H. Kim “*Observation of terahertz emission from a single layer graphene,*” KPS 2012, Pyeongchang, Korea, 24–26 October, 2012.
22. Y. M. Bahk, G. Ramakrishnan, J. H. Choi, H. R. Park, Y. H. Kim, K. J. Ahn, P. C. M. Planken, and D. S. Kim “*Surface plasmon-enhanced terahertz emission from single layer graphene,*” IRMMW–THz 2012, University of Wollongong, Australia, 23–28 September, 2012.
23. H. R. Park, Y. M. Bahk, K. J. Ahn, Q.–H. Park, D. S. Kim, L. Martin–Moreno, F. J. Garcia–Vidal, and J. Bravo–Abad

*“Strong coupling between nano-slot antenna and nano-object below skin-depth limit,”* NFO-12, Donostia-San Sebastian, Basque Country, Spain, 3–7 September, 2012.

24. H. R. Park, Y. M. Bahk, K. J. Ahn, Q.-H. Park, D. S. Kim, L. Martin-Moreno, F. J. Garcia-Vidal, and J. Bravo-Abad “Terahertz wave control enabled by nano objects embedded in slot antennas,” CLEO: 2012, San Jose, USA, 6–11 May, 2012.
25. H. R. Park, Y. M. Bahk, K. J. Ahn, Q.-H. Park, D. S. Kim, L. Martin-Moreno, F. J. Garcia-Vidal, and J. Bravo-Abad “Millimeter wave transmission control enabled by nanoscale objects embedded in nano slot antennas,” Nanolight, Benasque, Spain, 11–17 March, 2012.
26. Y. M. Bahk, J. W. Choi, H. R. Park, J. S. Kyoung, K. J. Ahn, and D. S. Kim “Anomalous dipole coupling of terahertz plasmonic nanoresonators,” Nanolight, Benasque, Spain, 11–17 March, 2012.
27. H. R. Park, Y. M. Bahk, J. Bravo-Abad, J. H. Choe, Q.-H. Park, K. J. Ahn, F. J. Garcia-Vidal, and D. S. Kim “Millimeter wave transmission control enabled by nanoscale objects embedded in nano slot antennas,” THz-Bio Workshop 2012, Engineer House, Seoul National University, Seoul, Korea, 6–8 February, 2012.
28. Y. M. Bahk, J. W. Choi, J. S. Kyoung, K. J. Ahn, and D. S. Kim “Modulation of transmission resonance by coupling of asymmetric two terahertz plasmonic nanoantennas,” THz-Bio Workshop 2012, Engineer House, Seoul National University, Seoul, Korea, 6–8 February, 2012.
29. D. S. Kim, W. S. Bahk, S. H. Eah, H. W. Kihm, Q. W. Kihm, H. R. Park, J. S. Kyoung, Y. G. Jeong, Y. M. Bahk, and T. H. Kang “Single Nanohole: Polarization analyzer for magnetic component of the light,” KPS 2011, Busan, Korea, 19–21 October, 2011.

30. H. R. Park, Y. M. Bahk, J. Bravo-Abad, J. H. Choe, Q.-H. Park, K. J. Ahn, F. J. Garcia-Vidal, and D. S. Kim “*Strong coupling between slot antennas separated by sub-skin depth barriers,*” IRMMW-THz 2011, Houston, TX, USA, 2–7 October, 2011.
31. Y. M. Bahk, H. R. Park, H. S. Kim, Q.-H. Kim, S. H. Lee, W. S. Park, J. Y. Rhie, K. J. Ahn, D. S. Kim, J. Bravo-Abad, and F. J. Garcia-Vidal “*Anomalous band formation of transmission through terahertz nanoantennas,*” KPS 2011, Daejeon, Korea, 13–15 April, 2011.
32. J. S. Kyoung, S. B. Choi, H. S. Kihm, H. R. Park, Y. G. Jeong, Y. M. Bahk, B. J. Kim, H. T. Kim, K. J. Ahn, and D. S. Kim “*Nanoresonator enabled terahertz all-optical switching on vanadium dioxide thin film,*” KPS 2011, Daejeon, Korea, 13–15 April, 2011.
33. Y. M. Bahk, H. R. Park, S. H. Lee, K. J. Ahn, H. S. Kim, D. S. Kim, Y. H. Ahn, J. Bravo-Abad, L. Martin-Moreno, and F. J. Garcia-Vidal “*Anomalous band formation of transmission through terahertz nanoantennas,*” THz-Bio Workshop 2011, Hoam Faculty House, Seoul National University, Seoul, Korea, 19–20 January, 2011.
34. H. R. Park, Y. M. Park, Q.-H. Kim, Y. G. Jeong, J. H. Choe, S. H. Han, O. K. Suwal, S. S. Choi, K. J. Ahn, N. K. Park, Q.-H. Park, and D. S. Kim “*Terahertz wave transmission control enabled by nanoscale metallic particles below the skin-depth limit,*” THz-Bio Workshop 2011, Hoam Faculty House, Seoul National University, Seoul, Korea, 19–20 January, 2011.
35. H. R. Park, Y. M. Park, J. H. Choe, S. H. Han, O. K. Suwal, S. S. Choi, K. J. Ahn, N. K. Park, Q. Park, and D. S. Kim “*Control of terahertz nanoresonator by a single metallic nanorod,*” KPS 2010, phoenixpark, Korea, 20–22 October, 2010.
36. D. H. Choi, H. R. Park, Y. M. Park, and G. S. Park

- “Polarization dependent terahertz band pass filters with asymmetric cross shaped hole arrays,”* IRMMW–THz 2010, Angelicum, Rome, Italy, 5–10 September, 2010.
37. H. R. Park, S. M. Koo, Y. M. Park, M. A. Seo, O. K. Suwal, Q. Park, S. S. Choi, N. K. Park, K. J. Ahn, and D. S. Kim “*Pinch harmonic analogue of terahertz nanoresonator control using metal nano-rods,*” IRMMW–THz 2010, Angelicum, Rome, Italy, 5–10 September, 2010.
38. H. R. Park, S. M. Koo, O. K. Suwal, Y. M. Park, J. S. Kyoung, M. A. Seo, S. S. Choi, N. K. Park, D. S. Kim, and K. J. Ahn “*Resonance frequency shifts of rectangular holes on finite dielectric substrates,*” IRMMW–THz 2010, Angelicum, Rome, Italy, 5–10 September, 2010.
39. Y. M. Park, H. R. Park, H. S. Kim, J. S. Kyoung, K. J. Ahn, and D. S. Kim “*Tight-binding description of transmission through crowded terahertz nanoresonators,*” IRMMW–THz 2010, Angelicum, Rome, Italy, 5–10 September, 2010.
40. Y. M. Park, H. R. Park, H. S. Kim, J. S. Kyoung, M. A. Seo, K. J. Ahn, and D. S. Kim “*Band formation of transmission through crowded terahertz nano antennas,*” The Plasmonics Gordon Research Conference 2010, Colby College, Waterville, ME, USA, 13–18 June, 2010.
41. H. R. Park, Y. M. Park, H. S. Kim, J. S. Kyoung, M. A. Seo, D. J. Park, Y. H. Ahn, K. J. Ahn, and D. S. Kim “*Nearly-perfect ultrabroadband transmission of log-periodic terahertz nanoresonators,*” The Plasmonics Gordon Research Conference 2010, Colby College, Waterville, ME, USA, 13–18 June, 2010.
42. H. R. Park, Y. M. Park, H. S. Kim, J. S. Kyoung, M. A. Seo, K. J. Ahn, and D. S. Kim “*Perfect transmission of terahertz waves in periodic nanogap antennas,*” The 7<sup>th</sup> Asia–Pacific Conference on Near–field Optics (APNFO–7), Jeju, Korea, 25–27 November, 2009.

43. Y. M. Park, H. R. Park, H. S. Kim, J. S. Kyoung, M. A. Seo, Y. G. Jeong, K. J. Ahn, and D. S. Kim “*Broadband terahertz transparency of metamaterials using nano-antennas,*” KPS 2009, Changwon, Korea, October 21–23, 2009.